Spin Observables in η Meson Photoproduction on the Proton

by

Ross Tucker

A Dissertation Presented in Partial Fulfillment
of the Requirements for the Degree
Doctor of Philosophy

Approved April 2016 by the
Graduate Supervisory Committee:

Barry Ritchie, Chair
Michael Dugger
Ricardo Alarcon
Richard Lebed

ARIZONA STATE UNIVERSITY

May 2016

ABSTRACT

A series of experiments using a polarized beam incident on a polarized frozen spin target (FROST) was conducted at Jefferson Lab in 2010. Results presented here were taken during the second running period with the FROST target using the CEBAF Large Acceptance Spectrometer (CLAS) detector at Jefferson Lab, which used transversely-polarized protons in a butanol target and a circularly-polarized incident tagged photon beam with energies between 0.62 and 2.93 GeV. Data are presented for the F and T polarization observables for η meson photoproduction on the proton from $W = 1.55$ GeV to 1.80 GeV. The data presented here will improve the world database and refine theoretical approaches of nucleon structure.

ACKNOWLEDGMENTS

First, I would like to thank Professor Barry Ritchie, without whom none of this would be possible. Special thanks go out to Associate Research Professor Michael Dugger. I would also like to thank dissertation committee members Professors Ricardo Alarcon and Richard Lebed. My parents and Fran O'Rourke set me on my journey. Ed Ihrig and John Shumway inspired me. Joshua Choi and Surani Joshua caught me when I stumbled. Finally, I would like to thank the National Science Foundation for providing the funding that allowed me to pursue and achieve this degree (grants PHY-09693201 and PHY-1306737).

TABLE OF CONTENTS

Page

LIST OF TABLES v

LIST OF FIGURES vi

CHAPTER

1 INTRODUCTION 1

2 BACKGROUND 6

2.1 The Nucleon Excitation Spectrum 6

2.2 The Helicity Amplitude Matrix 11

2.3 Observables 13

2.4 The Bremsstrahlung Process 14

2.5 Møller Scattering [17] 16

2.6 Dynamic Nuclear Polarization 17

3 EXPERIMENTAL APPARATUS AND TECHNIQUES 21

3.1 The Continuous Electron Beam Accelerator Facility (CEBAF) 22

3.2 The Møller Polarimeter [21] 24

3.3 The Hall B Bremsstrahlung Tagging Facility [21, 22] 26

3.4 The CEBAF Large Acceptance Spectrometer (CLAS) [21] 28

3.5 The FROzen Spin Target (FROST) 33

3.6 Data-acquisition System (DAQ) Trigger 34

3.7 Summary 35

4 DATA ANALYSIS 36

4.1 Details of Technique 37

5 RESULTS 55

5.1 ETA-MAID Model 55

5.2 Observables T and F 56

5.3 Excitation Plots 56

CHAPTER Page

6 CONCLUSIONS 62

6.1 Future Work 62

REFERENCES 63

APPENDIX 66

A T OBSERVABLE FOR η PHOTOPRODUCTION 67

B F OBSERVABLE FOR η PHOTOPRODUCTION 69

LIST OF TABLES

Table Page

2.1 Baryon Summary Tables for $N^\star$ and Δ Resonances 8

2.2 All Possible Pseudoscalar Photoproduction Spin Observables 11

2.3 Helicity Amplitude Matrix Elements 12

2.4 Observable Decompositions in Helicity Amplitudes 13

4.1 Reaction Signature Cuts 43

4.2 Initial Seeds for Missing Mass Histogram Fit Functions 51

4.3 Indices for the Possible Beam and Target Orientations 54

A.1 T Observable for η Photoproduction 68

B.1 F Observable for η Photoproduction 70

LIST OF FIGURES

Figure		Page
1.1	Standard Model of Elementary Particles	2
2.1	Nucleon Resonances Predicted by One Quark-Based Model	7
2.2	Total Photoproduction Cross Sections for $\gamma p \to \pi^+ n$	9
2.3	Total Photoproduction Cross Sections for Resonances Inferred for $\gamma p \to p\eta$	10
2.4	Hypothetical Møller Polarimeter Electron Signal	18
2.5	Model of the Dynamic Nuclear Polarization (DNP) Process	19
2.6	Polarization Fraction as a Function of Time	19
3.1	Photograph of CEBAF and Schematic Diagram of Detector	23
3.2	One of the Linear Accelerators in CEBAF	24
3.3	Bending Arc Magnets in the CEBAF Accelerator	25
3.4	Schematic of the Møller Polarimeter	26
3.5	Schematic of the Photon Tagger	27
3.6	Schematic Cross Section of the CLAS Detector	29
3.7	Profile of the CLAS Magnetic Field Strength	30
3.8	Cross Section of the Start Counter	31
3.9	Part of a Drift Chamber in Region Three	32
3.10	The FROST Target	34
4.1	2-d Missing Mass vs Azimuthal Angle	40
4.2	Vertex Position Distribution	41
4.3	Integrated Missing Mass Spectrum for Each Reaction Signature	44
4.4	Example Fit of Phi Offset Angle	45
4.5	Distribution of Target Polarization Fractions	47

Figure Page

4.6 Distribution of Photon Beam Polarizations 48
4.7 Example Missing Mass Plot Demonstrating Kinematic Shoulder 50

5.1 T Observable vs $\cos\theta$ 58
5.2 F Observable vs $\cos\theta$ 59
5.3 T Observable vs W 60
5.4 F Observable vs W 61

Chapter 1

INTRODUCTION

The Standard Model of particle physics is believed to explain almost every observed natural phenomenon excluding gravity. The model proposes that all matter and energy can be represented as quantum mechanical fields corresponding to particles. Forces are explained as a consequence of the exchange of force-carrying particles, which are called gauge bosons. The particles of the Standard Model are shown in Figure 1.1. Almost all matter (by mass) is composed of systems of two or more quarks. Quarks come in six "flavors"; in order of increasing mass: up, down, strange, charm, bottom, and top (u, d, s, c, b, and t). Quarks interact with each other through the strong, weak, and electromagnetic forces.

The interaction of greatest strength between quarks is the strong nuclear interaction; this is the force which binds quarks together into nucleons and, indirectly, binds nucleons into nuclei. The force carrier boson for the strong nuclear force is the gluon, g. Just as the electromagnetic force couples to the electric charge, the strong force couples to a color charge given as red, green, or blue. Each flavor of quark has an associated anti-quark with the same mass but opposite internal quantum numbers, including anti-color. No free quarks have ever been observed — they are always bound into composite particles. Additionally, all observed composite particles are color singlets, which carry no net color charge.

Composite particles that feel the strong nuclear force are called "hadrons". Protons and neutrons are not the only hadrons, though the proton is the only stable one. Hadrons composed of three quarks are called "baryons" (Greek *barys*="heavy"), while hadrons composed of two quarks are called "mesons" (Greek *mesos*="intermediate"). As discussed above, the color charge for all baryons is a mixture of red, green, and blue charge such

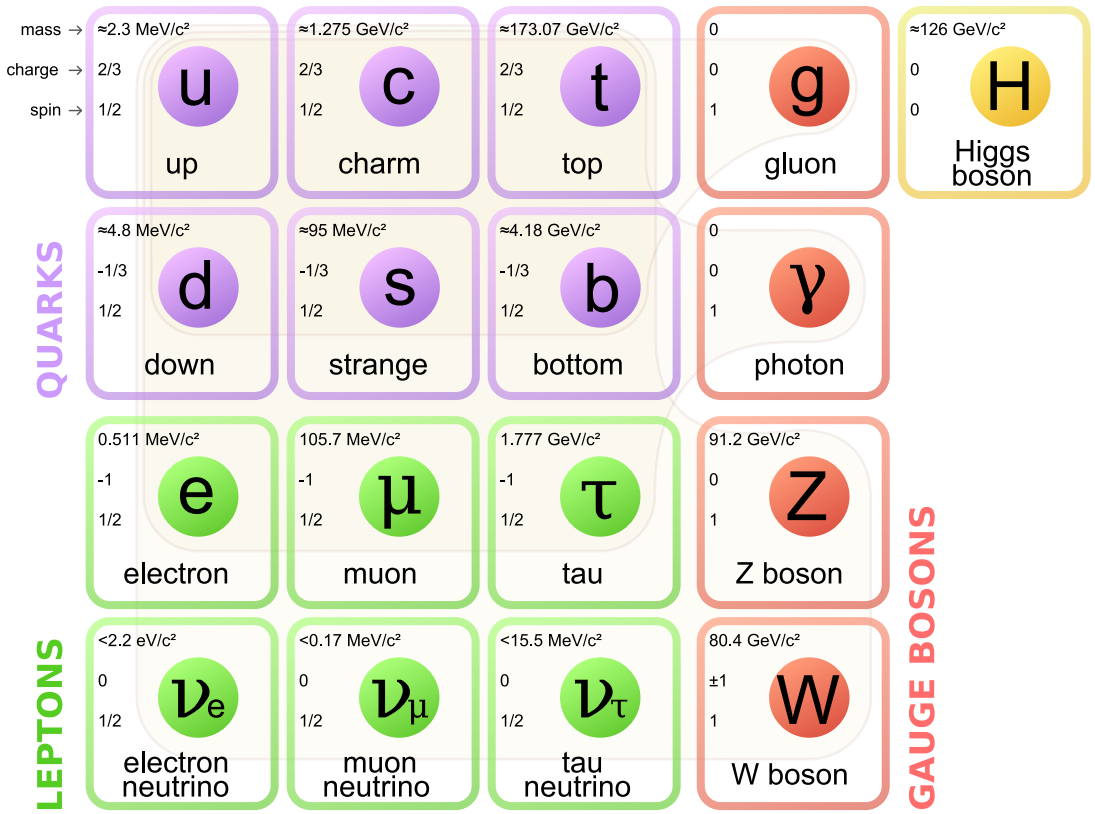

Figure 1.1: The fundamental constituents of matter and the interaction bosons in the Standard Model[1].

that the net color charge is zero. Mesons carry color on the quark, and anti-color on the anti-quark, such that the net color charge is zero. Searches are underway for more exotic combinations of quarks and gluons such as zero-quark "glueballs" or particles with four or more quarks, the four-quark "tetraquark" or five-quark "pentaquark". (In 2014, the LHCb collaboration reported a tetraquark candidate at 4430 MeV/c^2 (with suggested quark content $c\bar{c}d\bar{u}$) in $B^0 \to \psi' \pi^- K^+$ decays [2]. In 2016, the D0 collaboration reported a tetraquark candidate at 5568 MeV/c^2 (with suggested quark content of two quarks and two antiquarks of flavors b, s, u, d), though this state was disputed by the LHCb collaboration the next month [3, 4].)

In addition to the strong nuclear force, quarks carry electrical charge and interact electromagnetically. The electromagnetic and strong nuclear forces obey different functional

dependences on distance: the electromagnetic force decays as $\frac{1}{r^2}$ whereas the strong nuclear force increases with increasing distance. Therefore, when discussing relative strengths, it is important to specify the length scale under consideration. The strong nuclear force between quarks inside a hadron is on the order of 60 times the strength of the electromagnetic force. Outside a hadron, the strong force still has a residual effect, much like electromagnetic forces between neutral atoms still exist in the form of van der Waals forces. For example, within the nucleus, the strong nuclear force binds protons and neutrons together. The residual strong nuclear force between protons within a nucleus is on the order of 20 times the strength of the electromagnetic force between protons. At length scale larger than an atomic nucleus (approximately several times 10^{-15} m), the strong nuclear force has nearly no effect.

The strong nuclear force affects protons and neutrons identically. Thus, with respect to the strong interaction, the proton and neutron can be considered to be different states of the same particle, the *nucleon*, distinguished by introduction of a quantum number called isospin. The isospin of the nucleon is $I = \frac{1}{2}$: the proton has a projection onto the isospin "3-axis" of $I_3 = +\frac{1}{2}$ and the neutron has a projection $I_3 = -\frac{1}{2}$. The isospin I may be determined for any type of hadron by counting the number of charge states $N_Q = 2I + 1$. The isospin projection I_3 is given by the formula

$$I_3 = \frac{1}{2}\left((n_u - n_{\bar{u}}) - (n_d - n_{\bar{d}})\right),$$

where n_q is the number of quarks with flavor q. The lightest pseudo-scalar meson with zero isospin is the η meson. There are two such combinations of the three lighest quarks, $\eta_1 = \frac{u\bar{u}+d\bar{d}+s\bar{s}}{\sqrt{3}}$ and $\eta_8 = \frac{u\bar{u}+d\bar{d}-2s\bar{s}}{\sqrt{6}}$. The subscripts indicate that η_1 is a singlet and η_8 belongs to an octet. Because these two eigenstates share the same quantum numbers, there is mixing in the physically observed states. That is, the η_1 and η_8 states combine according

to the formula

$$\begin{pmatrix} \cos\theta_{\mathrm{P}} & -\sin\theta_{\mathrm{P}} \\ \sin\theta_{\mathrm{P}} & \cos\theta_{\mathrm{P}} \end{pmatrix} \begin{pmatrix} \eta_8 \\ \eta_1 \end{pmatrix} = \begin{pmatrix} \eta \\ \eta' \end{pmatrix},$$

where the mixing angle $\theta_P = -11.5^\circ$. This mixing angle must be determined phenomenologically-it cannot be derived from first principles [5]. The physically observed mesons are the η (mass $547.862 \pm 0.018\,\mathrm{MeV/c^2}$) and η' (mass $957.78 \pm 0.06\,\mathrm{MeV/c^2}$). The η meson is central to this dissertation. The η' meson was not produced in sufficient numbers to analyze for this dissertation and will not be discussed further.

With discovery of the Higgs boson in 2012, electroweak unification received an important confirmation. This theory suggests that the electromagnetic force (carried by the photon γ) and the weak force (carried by the $W^{\pm}$ bosons and the Z^0 boson) are manifestations of a single force dubbed the "electroweak" force, mediated by hypothetical W_3 and B bosons. The next step, uniting the electroweak and strong nuclear forces, is out of reach at the present time, in part because current understanding of the strong nuclear force is not yet unambiguous, so extrapolating to a higher energy scale is particularly risky. The electromagnetic force and the weak force can be analyzed with Feynman series approximation methods because the coupling constants for these forces are less than 1, so the terms in the Feynman series rapidly decrease. Series approximation methods for the strong nuclear force are often impossible because the coupling constant is greater than 1 and therefore series expansions diverge. If physics is to obtain a complete understanding of the fundamental forces, further research on the strong nuclear force is necessary.

In order to improve understanding of the strong nuclear force, one major research approach is the study of baryon resonances. Specifically, elucidating and understanding the excitation spectrum of the nucleon (proton or neutron) will increase understanding of the strong force interactions between the constituent quarks. This approach, called baryon

spectroscopy, is motivated by the successes of optical spectroscopy in the 19th and 20th centuries, which contributed significantly to the development of a quantum mechanical understanding of atoms and molecules in terms of quantum electrodynamics. As will be discussed in chapter 2, baryon spectroscopy is more challenging than atomic spectroscopy. One technique to overcome these challenges is to use spin observables, defined in Chapter 2, to supplement cross section data. Incorporating more observables makes it possible to more completely determine which resonances participate in a particular reaction. Two such observables are T and F.

The goal of this dissertation is to provide data on the spin observables T and F using data collected at Jefferson National Laboratory in order to help clarify the nucleon excitation spectrum and improve understanding of the strong nuclear force. In Chapter 2, these observables are defined mathematically along with other relevent theoretical quantities. Chapter 3 describes the experimental apparatus which was used to collect the data analyzed in this dissertation. Chapter 4 explains the method used for the data analysis process. Chapter 5 contains the results of the analysis. Chapter 6 discusses the implications of the results and what future measurements are required.

Chapter 2

BACKGROUND

In this chapter, the basic physics topics which provide the background for obtaining and interpreting the results of this work are presented. First, the nucleon excitation spectrum is described, and the advantages of η meson photoproduction are demonstrated. Second, the observables T and F are derived from the scattering matrix. Third, the observables are connected to measured quantities. Fourth, the bremsstrahlung process, which was used to generate the beam of high-energy photons, is described. Fifth, the Møller scattering process which was used to measure the polarization of the electron beam is described. Sixth, the dynamic nuclear polarization technique that was used in the experimental target is described.

2.1 The Nucleon Excitation Spectrum

The strong interaction is described in the theory of quantum chromodynamics (QCD) using the Lagrangian

$$\mathscr{L}_{\mathrm{QCD}} = \bar{\psi}_i \left(i \left(\gamma^\mu D_\mu \right)_{ij} - m\delta_{ij} \right) \psi_j - \frac{1}{4} G^a_{\mu\nu} G^{\mu\nu}_a \,,$$

where $\psi_i(x)$ is the quark field, γ^μ are the Dirac matrices, D_μ is the covariant derivative, and $G^a_{\mu\nu}$ represents the gluon field-strength tensor. No single approach has yet proven to be able to analytically solve the QCD Lagrangian, so there is as yet no unified model for hadronic structure.

Most quark-based QCD models and lattice QCD simulations predict many more resonances than have been experimentally observed, one example of which is illustrated in

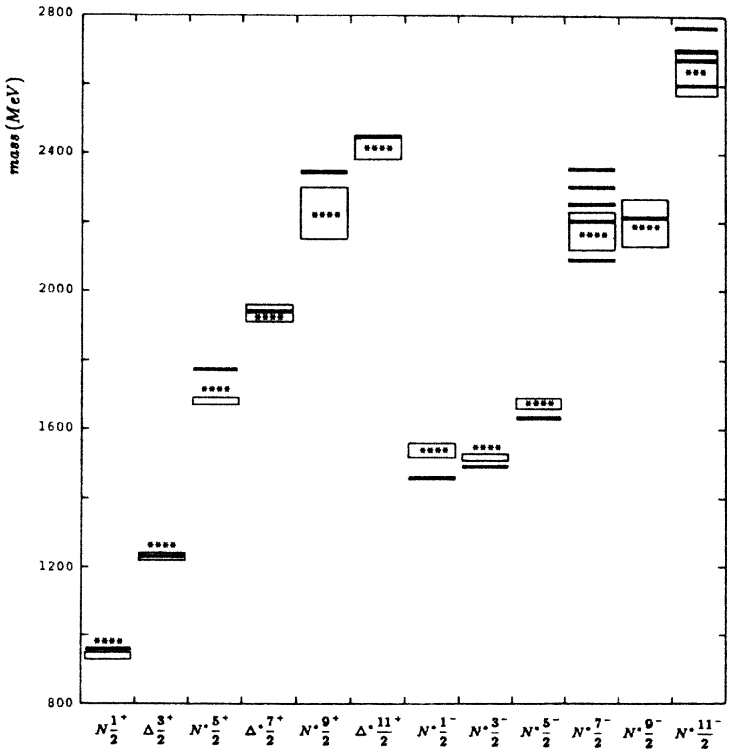

Figure 2.1: Missing nucleon resonances predicted by a particular quark-based model are shown with bars. States known at the time are shown with boxes [6]. Since publication of this model, one of the predicted states has been discovered while others remain unobserved. In particular, an $N^\star$ state with $J^P = \frac{5}{2}^+$ was identified in 2012 with mass 1860 MeV/c^2, though it is only rated at two stars in the 2014 Particle Data Group review. The several additional $N^\star$states with $J = \frac{7}{2}$ and $J = \frac{11}{2}$ have still not been observed.

Figure 2.1 [6]. Furthermore, many of the states that have been observed need better evidence, and the important properties of those states are often poorly known. The Particle Data Group (PDG) for 2015 lists 28 $N^\star$ nucleon resonances with $I = \frac{1}{2}$, of which 13 are ranked as having "fair" or "poor" evidence of existence. The Δ nucleon resonances with $I = \frac{3}{2}$ are in even worse shape, with 12 of 22 states ranked as "fair" or "poor". Table 2.1 shows the current status of these 30 resonances [7]. The 2015 Nuclear Science Advisory Commitee Long Range Plan highlighted Jefferson Lab's plans to explore hadronic structure as the first point in their first recommendation [8].

Resolving the baryon excitation spectra into constituent resonance states is nontrivial. For example, Figure 2.2 illustrates some of the resonances predicted to participate in the

Table 2.1: Baryon summary table of the $N^\star$ (upper table) and Δ (lower table) resonances, where the number represents the mass in MeV$/c^2$ and the stars are the 2014 Particle Data Group ratings [7].

1440	★★★★	1700	★★★	1900	★★★	2190	★★★★
1520	★★★★	1710	★★★	1990	★★	2220	★★★★
1535	★★★★	1720	★★★★	2000	★★	2250	★★★★
1650	★★★★	1860	★★	2040	★	2300	★★
1675	★★★★	1875	★★★	2060	★★	2570	★★
1680	★★★★	1880	★★	2100	★	2600	★★★
1685	★	1895	★★	2120	★★	2700	★★
1232	★★★★	1905	★★★★	2000	★★	2400	★★
1600	★★★	1910	★★★★	2150	★	2420	★★★★
1620	★★★★	1920	★★★	2200	★	2750	★★
1700	★★★★	1930	★★★	2300	★★	2950	★★
1750	★	1940	★★	2350	★		
1900	★★	1950	★★★★	2390	★		

reaction $\gamma p \to \pi^+ n$. There are many broad, overlapping states. States are broad because the short lifetime of an excited state requires a broad energy width by the uncertainty principle: $\Delta E\,\Delta t \sim \hbar$. Strong force interactions typically have $\Delta t \sim\ 10^{-23}$ s; thus $\Delta E \sim\ 200$ MeV.

One way to clarify this spectrum is to use the fact that strong interactions conserve isospin. The process $\gamma p \to p\eta$ provides an isospin filter: since the η meson has $I = 0$, there can be no contribution from Δ ($I = \frac{3}{2}$) resonances. Mathematically, the isospin filter mechanism is a consequence of the Clebsch-Gordan decomposition of isospin. Let $|I\,I_3\rangle$ represent the isospin ket of a particle, where I is the isospin and I_3 is the isospin projection. A reaction with an isospin-1 meson such as $\gamma p \to \pi^+ n$ has decomposition

$$\left|\pi^+\right\rangle \otimes |n\rangle = |1\,1\rangle \otimes \left|\frac{1}{2}\,-\frac{1}{2}\right\rangle = \sqrt{\frac{1}{3}}\left|\frac{3}{2}\,\frac{1}{2}\right\rangle \oplus \sqrt{\frac{2}{3}}\left|\frac{1}{2}\,\frac{1}{2}\right\rangle = \sqrt{\frac{1}{3}}\,|\Delta\rangle \oplus \sqrt{\frac{2}{3}}\,|N^\star\rangle\ .$$

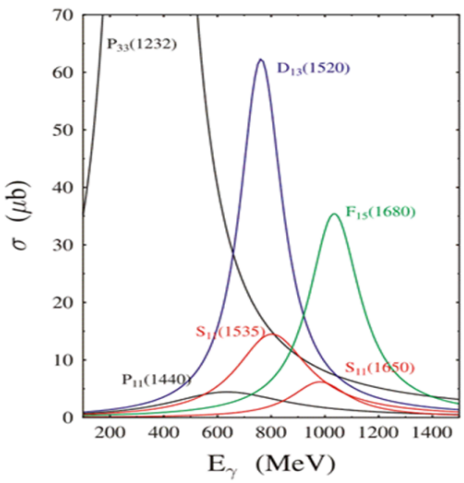

Figure 2.2: Total photoproduction cross sections for resonances for $\gamma p \to \pi^+ n$ as a function of incident photon energy E_γ. Note that the πN channel couples to both $I = 1/2$ and $I = 3/2$ resonances [9].

Note that since electric charge is conserved, the resonances in this case are positively charged. The first term on the right hand side represents a coupling to a Δ^+ resonance because it has $I = \frac{3}{2}$. The second term on the right hand side represents a coupling to $N^\star$ states because it has $I = \frac{1}{2}$. Thus, π meson photoproduction populates both $I = \frac{1}{2}$ and $I = \frac{3}{2}$ states, all of which must be disentangled.

On the other hand, a reaction such as $\gamma p \to p\eta$ has decomposition

$$|\eta\rangle \otimes |p\rangle = |00\rangle \otimes \left|\frac{1}{2}\,\frac{1}{2}\right\rangle = \left|\frac{1}{2}\,\frac{1}{2}\right\rangle = |N^\star\rangle \ ,$$

which lacks a coupling to Δ resonances (at least for single-step processes). This can greatly simplify the baryon excitation spectrum. Compare the π meson photoproduction resonance cross sections in Figure 2.2 to the η meson photoproduction resonance cross sections in Figure 2.3. The channel $\gamma p \to p\,\eta$ does not include any of the Δ resonances, so this channel provides an opportunity to disentangle fewer resonances at a time, with a sole focus on the $N^\star$ isospin-$\frac{1}{2}$ resonances.

Despite the utility of using a reaction with an isospin filter to disentangle the reso-

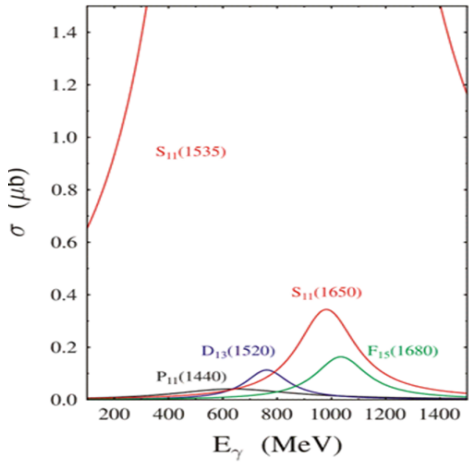

Figure 2.3: Total photoproduction cross sections for resonances inferred for $\gamma p \to p\eta$ as a function of incident photon energy E_γ. $I = 3/2$ resonances are absent for this reaction [9].

nances, few data beyond cross section measurements are presently available because the total cross sections for π meson channels are much larger than for η meson channels, and because η mesons do not carry electrical charge, making detection more difficult. Even so, a major experimental effort has taken place to clarify the nucleon excitation spectrum with a variety of channels, including η photoproduction. At ASU, this has been the focus of four successive doctoral dissertations, from 2001 to the present. These dissertations have established measurements for the cross section σ, the helicity asymmetry E, and the beam asymmetry Σ for η meson photoproduction from the proton [10, 11, 12].

Despite the advantages provided by the isospin filter, Figure 2.3 still illustrates that many overlapping states with cross sections of widely varying magnitudes are expected to be seen. Theoretical descriptions of many types benefit from using polarization observable data to supplement cross sections. A measurement of polarization observables allows theoretical models to better narrow down the resonance parameters of various models because it provides additional constraints which models must fulfill [13]. For that reason, a program of polarized photon beam / polarized proton target experiments have been performed at Jefferson Lab to disentangle nucleon resonances by measuring polarization observables.

Table 2.2: All possible pseudoscalar photoproduction spin observables and the experimental conditions for measuring each observable. Coordinates are defined as follows: $\hat{z}$ is the initial photon direction, $\hat{x}$ is in the reaction plane, and $\hat{y} = \hat{z} \times \hat{x}$. Primed coordinates are such that $\hat{z}'$ is in the direction of the emitted meson, $\hat{y}' = \hat{y}$, and $\hat{x}' = \hat{y} \times \hat{z}'$. The column labels "Target", "Recoil", and "Target+Recoil" refer to the polarizations needed for that experiment. The row labels "unpol[arized]", "linear", and "circular" refer to the photon beam polarization conditions required for that experiment.

Photon			Target			Recoil		Target+Recoil			
	-	-	-	-	x'	y'	z'	x'	x'	z'	z'
	-	x	y	z	-	-	-	x	z	x	z
unpol	σ_0	0	T	0	0	P	0	$T_{x'}$	$-L_{x'}$	$T_{z'}$	$T_{z'}$
linear	$-\Sigma$	H	$(-P)$	$-G$	$O_{x'}$	$(-T)$	$O_{z'}$	$(-L_{z'})$	$(T_{z'})$	$(-L_{x'})$	$(-T_{x'})$
circular	0	F	0	$-E$	$-C_{x'}$	0	$-C_{z'}$	0	0	0	0

For single pseudoscalar meson photoproduction, there are 8 possible helicity states, corresponding to the possible combinations of 4 initial and 2 final helicity states. That is, 8 complex amplitudes completely characterize the pseudoscalar meson photoproduction process for a given center-of-mass energy W. It can be shown that at least eight experiments are required to perform a 'complete' measurement for a given W [14]. A complete measurement is one which allows the scattering matrix (defined in section 2.2) to be completely specified. All possible observables for η meson photoproduction are listed in Table 2.2. In order to perform a complete experiment, there are conditions on the kinds of experiments which are needed: in particular, without measuring the recoil polarization, we can obtain only a 'nearly complete' measurement of this process.

2.2 The Helicity Amplitude Matrix

Mathematically, the origin of the spin observables shown in Table 2.2 is the scattering matrix. An overview of the derivation of T and F is helpful for a for deeper understanding. I start out by defining the four-momenta and helicities of the particles involved in η meson photoproduction as follows: let λ_x and p_x^μ be the helicity and Lorentz 4-vector with μ as

Table 2.3: Helicity amplitude matrix elements in terms of photon helicity λ_γ, final proton helicity λ_f, and initial proton helicity λ_i.

λ_γ	λ_f	λ_i	H_i
1	$-\frac{1}{2}$	$-\frac{1}{2}$	H_1
1	$-\frac{1}{2}$	$\frac{1}{2}$	H_2
1	$\frac{1}{2}$	$-\frac{1}{2}$	H_3
1	$\frac{1}{2}$	$\frac{1}{2}$	H_4
-1	$-\frac{1}{2}$	$-\frac{1}{2}$	H_4
-1	$-\frac{1}{2}$	$\frac{1}{2}$	$-H_3$
-1	$\frac{1}{2}$	$-\frac{1}{2}$	$-H_2$
-1	$\frac{1}{2}$	$\frac{1}{2}$	H_1

the spacetime index and lower index x represents the particle. In what follows, the index γ refers to the incident photon, the index i refers to the target proton, the index f refers to the recoil proton, and the index η refers the photoproduced η meson. The scattering matrix for η meson photoproduction can be written as

$$\mathbb{S} = 1 + i\,(2\pi)^4\,\delta^4\left(p^\mu_\eta + p^\mu_f - p^\mu_i - p^\mu_\gamma\right)\left(8\pi W\,\sqrt{16\,E_\gamma E_i E_f E_\eta}\right)\mathbb{A}\,, \tag{2.1}$$

where W is the center-of-mass energy given by $W = m_p c^2\sqrt{4E_\gamma^2+1}$ where m_p is the mass of the proton, and the amplitude $\mathbb{A}$ is a 2x2 matrix which contains spin information [14]. The matrix $\mathbb{A}$ connects initial and final spin states; its columns refer to initial nucleon spin and its rows refer to final nucleon spin. If the spins are chosen to be quantized along $\mathbf{p}_\eta$ and $\mathbf{p}_\gamma$ in the center-of-momentum frame, then the elements of $\mathbb{A}$ are the helicity amplitudes $A_{\alpha\beta}$, where $\alpha = -\lambda_\mathrm{f}$ gives the final total helicity, $\beta = \lambda_\gamma - \lambda_\mathrm{i}$ is the initial total helicity. The number of combinations of helicity orientations for the particles in this process is eight. Parity symmetry reduces the number of independent parameters to four, which are labeled as H_1,...H_4. The relationship between $A_{\alpha\beta}$ and H_i is given in Table 2.3. The helicity representation of each spin observable in Table 2.2 is shown in Table 2.4.

Table 2.4: Observables for single pseudoscalar photoproduction in terms of helicity amplitude [15].

Spin observable	Helicity representation
σ_0	$\frac{1}{2}\left(\lvert H_1\rvert^2+\lvert H_2\rvert^2+\lvert H_3\rvert^2+\lvert H_4\rvert^2\right)$
Σ	$\mathrm{Re}\left(-H_1H_4^\star+H_2H_3^\star\right)$
T	$\mathrm{Im}\left(H_1H_2^\star+H_3H_4^\star\right)$
P	$\mathrm{Im}\left(-H_1H_3^\star-H_2H_4^\star\right)$
G	$\mathrm{Im}\left(H_1H_4^\star-H_3H_2^\star\right)$
H	$\mathrm{Im}\left(-H_2H_4^\star+H_1H_3^\star\right)$
E	$\frac{1}{2}\left(\lvert H_1\rvert^2-\lvert H_2\rvert^2+\lvert H_3\rvert^2-\lvert H_4\rvert^2\right)$
F	$\mathrm{Re}\left(-H_2H_1^\star-H_4H_3^\star\right)$
O_x	$\mathrm{Im}\left(-H_2H_1^\star+H_4H_3^\star\right)$
O_z	$\mathrm{Im}\left(H_1H_4^\star-H_2H_3^\star\right)$
C_x	$\mathrm{Re}\left(H_2H_4^\star+H_1H_3^\star\right)$
C_z	$\frac{1}{2}\left(\lvert H_1\rvert^2+\lvert H_2\rvert^2-\lvert H_3\rvert^2-\lvert H_4\rvert^2\right)$
T_x	$\mathrm{Re}\left(-H_1H_4^\star-H_2H_3^\star\right)$
T_z	$\mathrm{Re}\left(-H_1H_2^\star+H_4H_3^\star\right)$
L_x	$\mathrm{Re}\left(H_2H_4^\star-H_1H_3^\star\right)$
L_z	$\frac{1}{2}\left(-\lvert H_1\rvert^2+\lvert H_2\rvert^2+\lvert H_3\rvert^2-\lvert H_4\rvert^2\right)$

Note the similarity between the expressions for T and F. This indicates that an analysis which simultaneously determines these observables will be sensitive to the phase between $H_1H_2^\star$ and $H_3H_4^\star$. The measurements of T and F presented in this work contribute to the body of data needed to determine the helicity amplitudes H_i.

2.3 Observables

The above cross section expressions are written using the outgoing meson trajectory to define one of the axes. The relation between center-of-mass energy W and incident photon

energy E_γ is given by

$$E_\gamma = \frac{\sqrt{W^2 - (m_p c^2)^2}}{2 m_p c^2}, \tag{2.2}$$

where m_p is the mass of the proton (938.27 MeV/c^2). In laboratory coordinates, the cross section for a circularly polarized beam on a transversely polarized target can be written using the equation

$$\frac{d\sigma}{d\Omega}\left(E_\gamma, \varphi\right) = \left(\frac{d\sigma}{d\Omega}\right)_0 \left(1 + P_\mathrm{t} T \sin\varphi + P_\mathrm{t} P_\gamma F \cos\varphi\right), \tag{2.3}$$

where the target asymmetry T and a double-polarization observable F are related to the cross section $\left(\frac{d\sigma}{d\Omega}\right)$ as a modulation in azimuthal angle φ of the unpolarized cross section $\left(\frac{d\sigma}{d\Omega}\right)_0$, with P_t (P_γ) being the degree of polarization for the target (incident photon).

The cross section in equation 2.3 is related to measured quantities by

$$\frac{d\sigma}{d\Omega} = \frac{Y_\eta}{N_\gamma \rho L \varepsilon}, \tag{2.4}$$

where $Y_\eta\left(E_\gamma, \theta, \varphi\right)$ is the η meson yield, $N_\gamma\left(E_\gamma\right)$ is the number of incident photons, ρ is the target density, L is the target length, and $\varepsilon\left(\theta, \varphi\right)$ is the overall detection efficiency for the particles measured in the final state.

2.4 The Bremsstrahlung Process

The bremsstrahlung process was used to generate a beam of high-energy photons for the experiment described in this dissertation. As a beam of electrons accelerates in the electromagnetic field of a target nucleus, photons are emitted. Olsen and Maximon derived the result that the polarization of the emitted photon beam is a function of the fractional energy transferred [16]. They obtained the result that the polarization of the photon is given by the equation

$$P_\gamma = P_e \frac{4\tilde{E} - \tilde{E}^2}{4 - 4\tilde{E} + 3\tilde{E}^2}, \tag{2.5}$$

where $\tilde{E} = \frac{E_\gamma}{E_e}$ is the ratio of the emitted photon energy E_γ to the incident electron energy E_e, and P_e was the electron beam linear polarization. A summary of this calculation is in order.

The electron wave function $\psi_\pm$ is modeled using the Sommerfeld-Maue equation in the high-energy limit

$$\psi_\pm = \frac{1}{\sqrt{2}} e^{\frac{i}{\hbar}\mathbf{p}_e \cdot \mathbf{r}} \left(1 - \frac{i m_e c^2}{2E_e} \alpha \cdot \nabla\right) \begin{pmatrix} 1 \\ \\ \sigma \cdot \mathbf{p}_e / 1 + \frac{E_e}{m_e c^2} \end{pmatrix} v F_\pm,$$

where $\mathbf{p}_e$ is the 3-momentum of the electron, $\mathbf{r}$ is the position of the electron, v is the Pauli spinor in the electron's rest frame, $\alpha \equiv \begin{pmatrix} 0 & \sigma \\ \\ \sigma & 0 \end{pmatrix}$ is the Dirac operator, σ are the Pauli spin matrices, and $F_\pm$ is the solution to the equation $\left(\nabla^2 + \frac{2i}{mc}\mathbf{p}_e \cdot \nabla - \frac{2\hbar E_e}{mc} V(\mathbf{r})\right) F = 0$, normalized such that $\lim_{\mathbf{r}\to 1} F(\mathbf{r}) = 1$.

The amplitude for bremsstrahlung is calculated using the expression

$$\mathbf{A} \cdot \mathbf{e}^\star = \left\langle \psi_{f,-} \middle| \alpha \cdot \mathbf{e}^\star e^{-\frac{i}{\hbar}\mathbf{p}_\gamma \cdot \mathbf{r}} \middle| \psi_{i,+} \right\rangle.$$

To leading order and using the high energy limit, this can be evaluated and yields the expression

$$\mathbf{A} \cdot \mathbf{e}^\star = \left\langle v_f \middle| \left(\frac{E_{e,i} + E_{e,f}}{m_e c^2}\right) \mathbf{J} \cdot \mathbf{e}^\star + i E_\gamma \sigma \times \mathbf{J} \cdot \mathbf{e}^\star \middle| v_i \right\rangle.$$

The vector $\mathbf{e} = \frac{1}{\sqrt{2}}(\hat{\mathbf{x}} \pm i\hat{\mathbf{y}})$ is for circular polarization, where the $+$ sign corresponds to right-hand circular polarization and the $-$ sign corresponds to left-hand circular polariza-

tion. The vector **J** is defined as

$$\mathbf{J} = \frac{4\pi a}{E_\gamma q^2} A \cdot \left\{ \frac{\mathbf{u}}{1+|\mathbf{u}|^2} - \frac{\mathbf{v}}{1+|\mathbf{v}|^2} + \hat{\mathbf{p}}_\gamma \left(\frac{1}{1+|\mathbf{u}|^2} - \frac{1}{1+|\mathbf{v}|^2} \right) \right\},$$

where **u** and **v** are the components of $\mathbf{p}_i$ and $\mathbf{p}_f$ which are perpendicular to $\mathbf{p}_\gamma$, and A depends on the screening approximation being used. Olsen and Maximon show that the screening term can be neglected and that the circular polarization of the bremsstrahlung photon from transversely polarized electrons is given by the equation

$$P_\gamma = P_e E_\gamma \frac{\varepsilon_i + \frac{1}{3}\varepsilon_f}{\varepsilon_i^2 + \varepsilon_f^2 - \frac{2}{3}\varepsilon_i \varepsilon_f}.$$

Finally, using energy conservation $E_\gamma = E_i - E_f$, the substitution $\tilde{E} = \frac{E_\gamma}{E_i}$ allows us to write the polarization in a convenient form:

$$P_\gamma = P_e \frac{4\tilde{E} - \tilde{E}^2}{4 - 4\tilde{E} + 3\tilde{E}^2}. \tag{2.5}$$

This expression is used in the data analysis below.

2.5 Møller Scattering [17]

As will be discussed in section 3.2, the polarization of the electron beam incident on the bremsstrahlung target (radiator) was measured with a polarimeter which utilizes the Møller scattering process. In Møller scattering, an asymmetry in the scattering of an incident polarized electron beam is produced by passing the beam through a ferromagnetic metal foil whose atoms have been oriented by magnetizing the foil. To lowest order, the cross section $\left(\frac{d\sigma}{d\Omega}\right)_{\text{Møller}}$ for Møller scattering of a transversely polarized electron beam on a

transversely polarized target in the center-of-mass frame is given by the equation

$$\left(\frac{d\sigma}{d\Omega}\right)_{\text{Møller}} = \frac{\alpha^2}{W^2}\cdot\left(\left(\frac{3+\cos^2\theta}{\sin^2\theta}\right)^2 - P_{\text{f}}P_e\right),$$

where α is the fine structure constant, P_{f} is the polarization of the magnetized foil target, θ is the scattering angle in the center-of-mass frame. At a particular scattering angle, the cross section expression can be solved for P_e, which yields the equation

$$P_e = \frac{1}{KP_{\text{f}}}\cdot\left(\frac{\left(\frac{d\sigma}{d\Omega}\right)_{\text{M}+} - \left(\frac{d\sigma}{d\Omega}\right)_{\text{M}-}}{\left(\frac{d\sigma}{d\Omega}\right)_{\text{M}+} + \left(\frac{d\sigma}{d\Omega}\right)_{\text{M}-}}\right). \tag{2.6}$$

where the $\pm$ sign indicates electrons at the detector aligned or anti-aligned with the positive target polarization direction and K is a constant which depends on the particular scattering angle at which the detectors are located. This equation was used to generate electron polarization values used in Equation 2.5. A sketch of the electron signal as a function of scattering angle measured in a hypothetical Møller polarimeter is shown in Figure 2.4. The upper figure shows the detected electron yield as a function of scattering angle θ. A background corresponding to electron-iron scattering can be seen. The peak yield measured on either side of the detector is used in the asymmetry equation 2.6. The lower figure in Figure 2.4 shows the asymmetry between two detectors on opposite sides of the beam as a function of scattering angle θ.

2.6 Dynamic Nuclear Polarization

Dynamic nuclear polarization (DNP) is a technique for polarizing the hydrogen nuclei of a suitable material by transferring the spin polarization from electrons in paramagnetic radicals using microwave radiation. As described in section 3.5, the process begins with polarizing the material in a magnetic field at very low temperature (< 1 K). This field results in complete polarization of the paramagnetic radicals. The target is then excited using

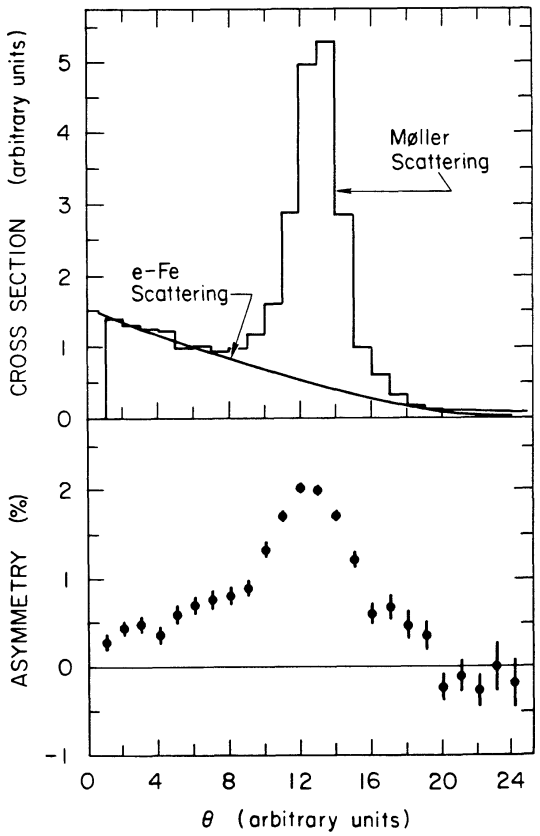

Figure 2.4: Hypothetical Møller polarimeter electron signal on one side of a detector. The upper figure shows the detected electron yield as a function of scattering angle θ. The lower figure shows the resulting asymmetry with the same axis as before [17].

microwave radiation with a frequency chosen to promote transfer from the electron orbital angular momentum to the nuclear spin. This microwave frequency is either slightly higher (lower) than the electron spin resonance frequency to transfer polarization parallel (anti-parallel) to the direction of the applied magnetic field, as illustrated in Figure 2.5. Once the target has reached a high polarization fraction, the microwave radiation and polarizing magnetic field are removed, and a small holding field is applied in order to maintain polarization during experimental data taking. A sketch of the polarization as a function of time is shown in Figure 2.6.

The basic process of radiation-induced polarization was first described by Albert Overhauser [19]. The process involves a simple transfer of polarization via cross-relaxation.

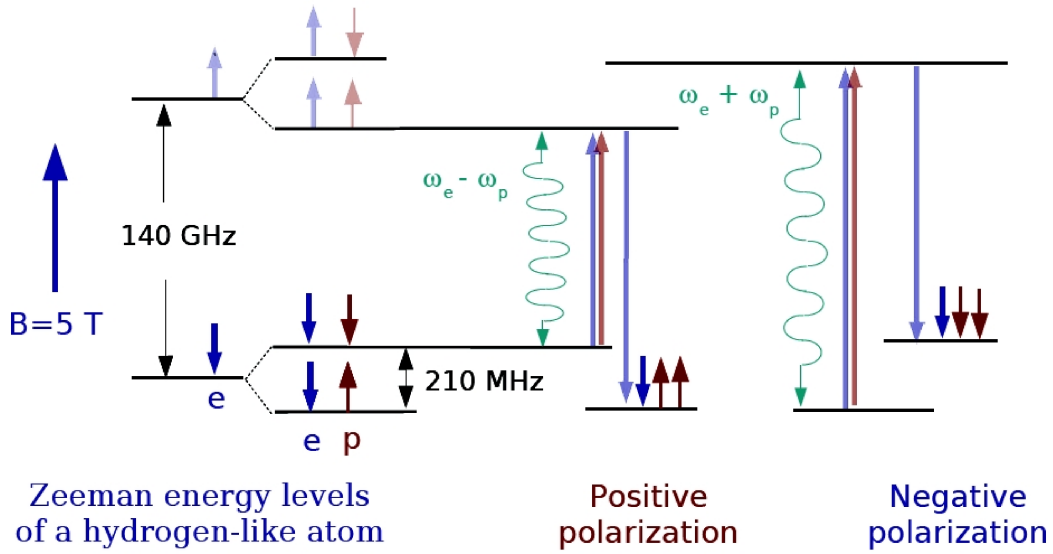

Figure 2.5: A diagram illustrating the dynamic nuclear polarization (DNP) process [12]. The static magnetic field polarizes the paramagnetic radicals. The energy gap to excite polarization is then a function of the proton spin-state gap (with characteristic Larmor frequency on the order of 210 MHz) and the electron spin-state gap (with characteristic Larmor frequency on the order of 140 GHz). Applied microwave radiation of a carefully chosen frequency was applied in order to stimulate transitions to the desired state, transferring polarization from the electronic spin to the nuclear spin.

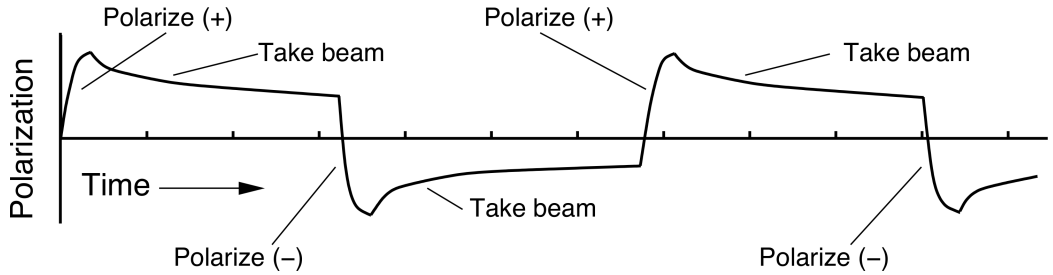

Figure 2.6: Polarization fraction as a function of time for the target used in this dissertation [18].

In particular, Overhauser predicted the spin transfer of a metal located in a constant magnetic field of magnitude B which is exposed to perpendicularly-polarized radiation with frequency $\omega_1 = \gamma_1 B$, where γ_1 is the electron gyromagnetic ratio. As discussed above, the target material in this experiment was a composite material. The electronic paramagnetic radicals are assumed to have Larmor frequency ω_1 as given above, while the target nuclei have Larmor frequency $\omega_2 = \gamma_2 B$, where γ_2 is the gyromagnetic ratio of the target. Spin coupling between spin $\mathbf{S}_1$ and $\mathbf{S}_2$ occurs via dipole-dipole interactions, as given by the

equation

$$U = -\frac{\mu_0 \gamma_1 \gamma_2}{4\pi r^3} \left(3 \left(\mathbf{S}_1 \cdot \hat{\mathbf{r}}\right) \left(\mathbf{S}_2 \cdot \hat{\mathbf{r}}\right) - \mathbf{S}_1 \cdot \mathbf{S}_2\right), \tag{2.7}$$

where U is the potential energy of the interaction, $\mu_0 = 4\pi \cdot 10^{-7}$ N/A^2 is the permeability of free space, and $\mathbf{r}$ is the displacement beween two dipoles.

The interaction given by Equation 2.7 allows for transfer of spin between internal spin and orbital spin when an external field of frequency $\Omega = \omega_1 \pm \omega_2$ is applied, where the $+$ sign results in spin-reversal in the anti-parallel configuration, and the $-$ sign results in spin-reversal in the parallel configuration. The transition probability for the opposite direction is suppressed to first order. Therefore, by applying microwave radiation of a particular frequency, there is a net polarization transfer from electrons to nuclei. The external magnetic field continues to "recharge" the electronic polarization. In theory, complete nuclear polarization is possible.

Chapter 3

EXPERIMENTAL APPARATUS AND TECHNIQUES

This chapter briefly documents the key pieces of apparatus and experimental techniques used to obtain the data required for the measurements in this work. All data for the Frozen Spin Target (FROST) experiment were obtained at the Thomas Jefferson National Accelerator Facility (Jefferson Lab) using the Continuous Electron Beam Accelerator Facility (CEBAF). The detector was the CEBAF Large Acceptance Spectrometer (CLAS), located within the John J. Domingo Experimental Hall B. CLAS was principally designed for the detection of charged particles.

Since the η meson has no electrical charge, the data from the reaction $\gamma p \to p\eta$ were analyzed by reconstructing the η meson 4-momentum by missing-mass techniques, aided when possible by the detection of decay products from the η meson itself. In this approach, the 4-momenta for the incoming photon and target and the outgoing recoil proton were needed to calculate the missing 4-momentum. The bremsstrahlung photon tagger provided the incoming photon energy information. The target proton was assumed to be at rest. The recoil proton momentum and the momenta for any other detected decay products were measured by CLAS.

Initially, the accelerator used to generate the high-energy electron beam used in this experiment is described. Second, the Møller polarimeter used to measure the polarization of the electron beam is described. Third, the bremsstrahlung tagger which was used to generate and measure the high-energy photon beam is described. Fourth, the CLAS detector used to detect the reaction products is described, with each of its major subsystems discussed in detail. Fifth, the polarized target is described. Sixth, the data-acquisition system configuration for data reduction is described.

3.1 The Continuous Electron Beam Accelerator Facility (CEBAF)

CEBAF is a superconducting electron accelerator with a "racetrack" geometry, as seen in Figure 3.1. At the time of this experiment, CEBAF could reach energies up to 6 GeV with energy resolution $\Delta E_e/E_e \leq 10^{-4}$. The charge distribution of the electron beam was that of pulses or "bunches" separated by approximately 2 ns. The electron source was a photocathode gun that could produce longitudinally polarized electron beams with polarizations of approximately 87%. This gun consisted of a GaAs cathode illuminated by a 1.497 GHz gain-switched diode laser. The frequency was chosen so that three pulses or "bunches" (one for each experimental hall) were produced every 2 ns. Gain-switching is a technique by which pulses of short duration were produced by biasing the laser near threshold and driving its medium above the lasing threshold with radiofrequency (rf) energy [20], A 5 MeV Mott polarimeter measured the electron polarization at the injector site.

Electrons emitted from the electron source entered the injector linear accelerator ("linac"), which boosted the energy of the electrons to 45 MeV before those particles entered the racetrack part of the accelerator. The injector linac and the main linac were composed of "cryomodules", which were four sets of paired superconducting-niobium radiofrequency cavities. The injector linac consisted of $2\,1/4$ cryomodules (or 9 cavities). The cavities were cooled to approximately 2 K with liquid helium to sustain superconductivity.

The racetrack consisted of two linacs, shown in Figure 3.2, each with 21 cryomodules of the type discussed above, with a total of 338 cavities in the entire racetrack. Each pass through one linac boosted the beam energy, with a maximum increase of approximately 800 MeV. The beam was recirculated between the two linacs, with the linacs connected by two 180° magnetic bending arcs of radius 80 m. The bending arcs contained five paths displaced vertically with a system of magnets, shown in Figure 3.3; the field strengths of the bending arc magnets were adjusted to produce the correct radius of curvature based

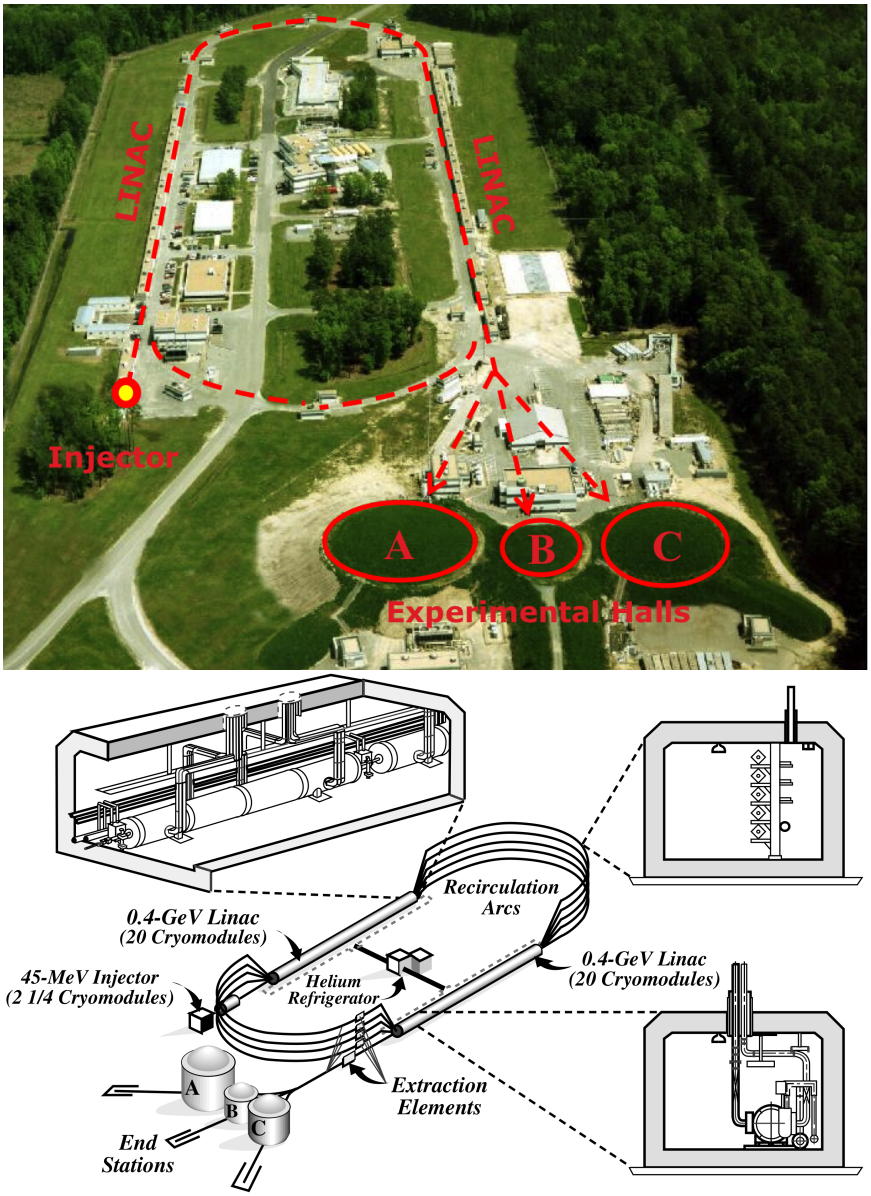

Figure 3.1: Above: A photograph of CEBAF from above as it looked at the time the data for this experiment were collected. The superimposed drawing illustrates several key components discussed in the text. Experimental halls are labelled A, B, and C. This work took data in Hall B. Below, a schematic diagram of CEBAF showing the components.

on the momentum carried by the electrons, which were deflected electromagnetically into the proper vertical bending track. For this experiment, the incident electron energy for the Hall B beam was 3.082 GeV. While CEBAF is capable of generating on the order of 1 μA of electron beam current, the electron beam current in Hall B was limited to between

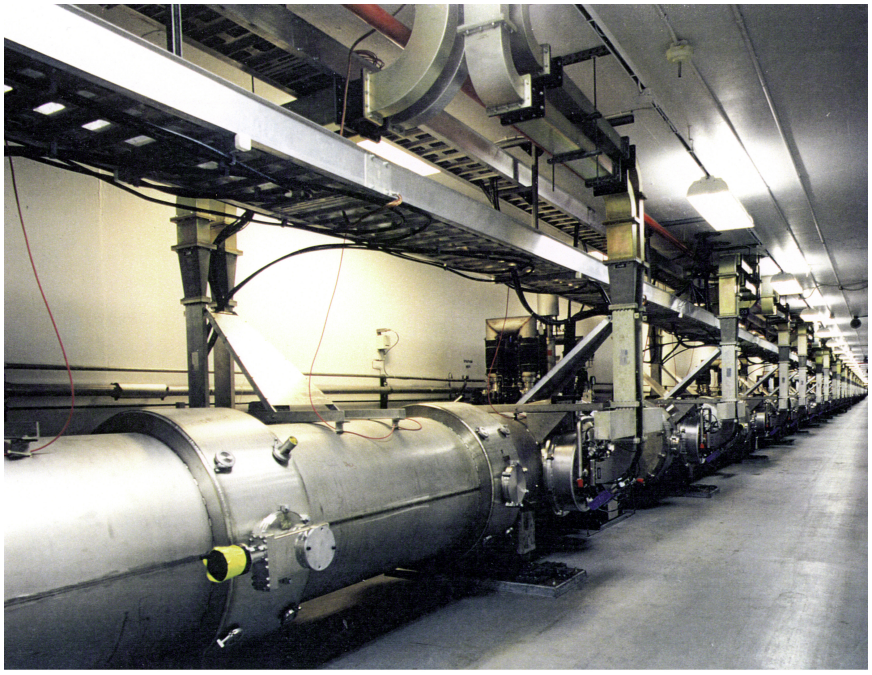

Figure 3.2: A portion of one of the two linear accelerators in CEBAF. The location of the two linear accelerators is shown in the schematic figure, Fig. 3.1 (bottom).

11.9 and 13.6 nA, due to the event-rate limitations of the detector systems in Hall B.

3.2 The Møller Polarimeter [21]

The polarization of the electron beam delivered to Hall B was measured several times during the experimental run period. This measurement was performed with a Møller polarimeter, which was located just upstream of the bremsstrahlung tagger described in the next section. A schematic diagram of this polarimeter is shown in Figure 3.4. The physics underlying this measurement was presented in section 2.5. The polarimeter consisted of a magnetized foil target, a pair of magnets, and two detectors. The target foil was 25 μm-thick permendur (a cobalt-iron alloy), and was magnetized by a Helmholtz coil capable of producing a field of approximately 10 mT. As electrons passed through the magnetized foil target, elastic electron-electron scattering resulted in an asymmetric scattering distribution measured by the two detectors, located 7 meters downstream of the target and 37.5 cm

Figure 3.3: Bending arc magnets in the CEBAF accelerator. Each magnet bends electrons of a specific momentum for that particular recirculation.

transverse to the beamline. The magnets were a pair of quadrupoles which separated the scattered electrons from the beam and deflected the electrons into the detectors.

The detectors consisted of lead and scintillating fibers. Data from the detector outputs were read by a scaler for each beam helicity state over the course of approximately 30 minutes. The polarization was then determined by the count asymmetry $A_{\text{Møller}}$ between the two detectors by the relation

$$A_{\text{Møller}} = \frac{N_+ - N_-}{N_+ + N_-},$$

where N_+ (N_-) is the number of positive (negative) helicity measurements made. It can be shown that the electron beam polarization is related to the count asymmetry by the equation

$$P_e \approx \frac{9A_{\text{Møller}}}{P_{\text{f}}},$$

where P_{f} is the polarization of the magnetized foil target [17]. Typical values of electron

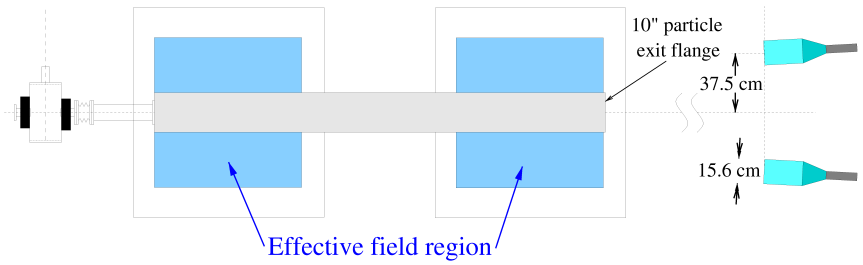

Figure 3.4: A schematic representation of the Hall B Møller polarimeter. Electron beam enters from left. The black bars on the left represent the entrance and exit flanges of the target region that contains the magnetized foil converter material.

beam polarization were approximately 87%, with a statistical uncertainty 1.5% (absolute). The uncertainty in this measurement is dominated by the uncertainty of the foil target polarization.

3.3 The Hall B Bremsstrahlung Tagging Facility [21, 22]

Photons for the experiment were produced by bremsstrahlung (the processed described in section 2.4 using the Hall B bremsstrahlung photon tagger.) Once inside Hall B, the electron beam struck a gold foil of thickness 10^{-4} radiation lengths. In the nuclear electric field of a gold atom in this foil radiator, an electron may experience bremsstrahlung with the subsequent emission of a photon with an energy E_γ given by the equation

$$E_\gamma = E_{e,i} - E_{e,f}\,,$$

where $E_{e,i}$ is the incoming electron beam energy and $E_{e,f}$ is the post-bremsstrahlung energy of the electron measured by the tagger. As described earlier, the energy of the incoming electron beam was well known, so the energy of each bremsstrahlung photon was determined by measuring the energy of the recoil electron that produced that photon.

The tagger system used a large C-frame room temperature iron magnet to deflect recoil electrons onto two arrays of scintillators. A schematic of the tagger is shown in Figure 3.5.

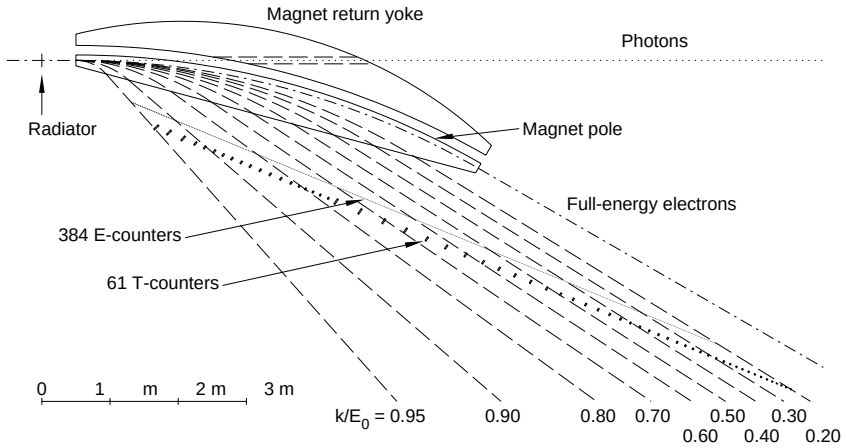

Figure 3.5: A schematic diagram of the Hall B photon tagger. The dashed lines represent electron trajectories, with the lowest energy electrons deflecting the greatest.

One plane of 384 plastic scintillators (called E-counters) were arranged in an overlapping pattern in order to measure the electron energy in 767 bins. Since electrons which have lost more energy were bent with a greater radius of curvature, the energy was determined by the counter that was hit. Electrons which did not radiate a bremsstrahlung photon were directed into a beam dump beneath the floor of Hall B.

The photon energy resolution for the tagger was $\Delta E_\gamma / E_\gamma = 10^{-3}$. The tagger system was capable of tagging photons with energies between 20% and 95% of the incident electron beam energy. For this experiment, this range corresponded to photon energy between 0.62 and 2.93 GeV.

In addition to the energy counters, the tagger system included an array of 61 timing counters ("T-counters"), with timing resolution better than 300 ps. The T-counters determine with which beam bunch the photon was associated. Downstream from the tagger system, the photon beam passed through a collimator that defined the size of the photon beam. Finally, sweep magnets eliminated charged particles generated from photons that struck the collimator walls.

The relative photon flux was estimated using techniques that will be described in section 3.5.

3.4 The CEBAF Large Acceptance Spectrometer (CLAS) [21]

CLAS was a large-acceptance detector with hexagonal symmetry that used a toroidal magnetic field. Figure 3.6 illustrates the detector geometry. Six superconducting NbTi/Cu coils generated a very uniform magnetic field between 0.3 and 1.2 T m between the superconducting coils, while leaving the target region field-free. The polar and radial profile of the magnetic field was designed so that forward-going particles (with typically higher momenta) passed through a stronger field. A diagram showing the relative magnetic field strength is shown in Figure 3.7. For this experiment, the direction of the magnetic field was such that positively-charged particles were bent away from the forward beam direction, and negatively charged particles were bent toward the forward beam direction.

Each superconducting coil consisted of four layers of 54 turns of conductor. The coils were wound without iron, so the total field was due entirely to current passing through the loops. For this experiment, the current was 1920 A. Superconductivity was accomplished by flowing super-critical helium through cooling tubes next to the windings. In the event of a superconductivity quench, the resistance of the copper limited the current to a safe level so that the magnet was not damaged.

3.4.1 Start Counter and Time-of-flight Subsystem [21, 23]

Two detector arrays within CLAS provided timing information for each event analyzed in this work. The time resolution for each component of these detector arrays was required to be between approximately $120 - 250$ ps. With such precision, it was possible to identify the CEBAF beam bunch, which had a very well-defined time. With the beam bunch identified, the ultimate uncertainty in time measurements was less than 25 ps.

The start counter was an array of scintillators positioned immediately outside the target in CLAS. Photomultiplier tubes were coupled to one end of each scintillator. These covered

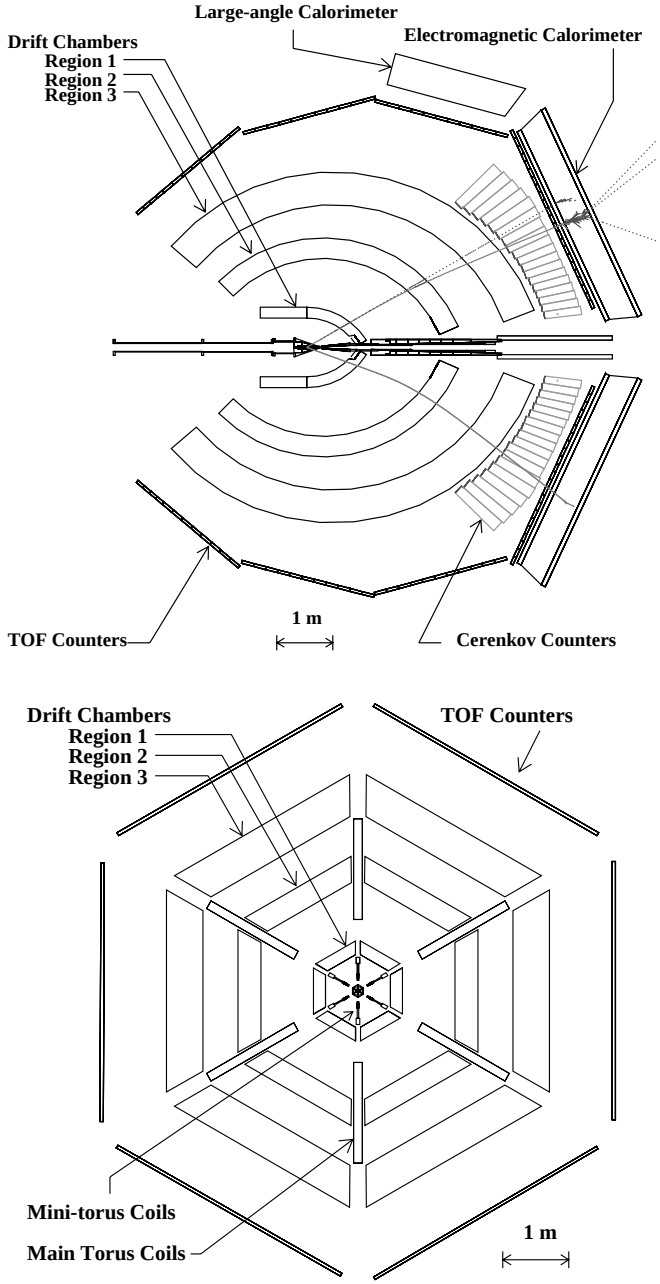

Figure 3.6: Schematic cross sections of the CLAS detector, illustrating the locations and arrangement drift chamber regions and TOF counters. On the top, a cross section top view. Example tracks for typical photon, electron, and proton are shown from top to bottom. The calorimeters and Čerenkov counters were not used for this analysis. On the bottom, a cross section perpendicular to beam. This view illustrates the positions of the superconducting magnet coils. The "Mini-torus" was only used in electron beam experiments.

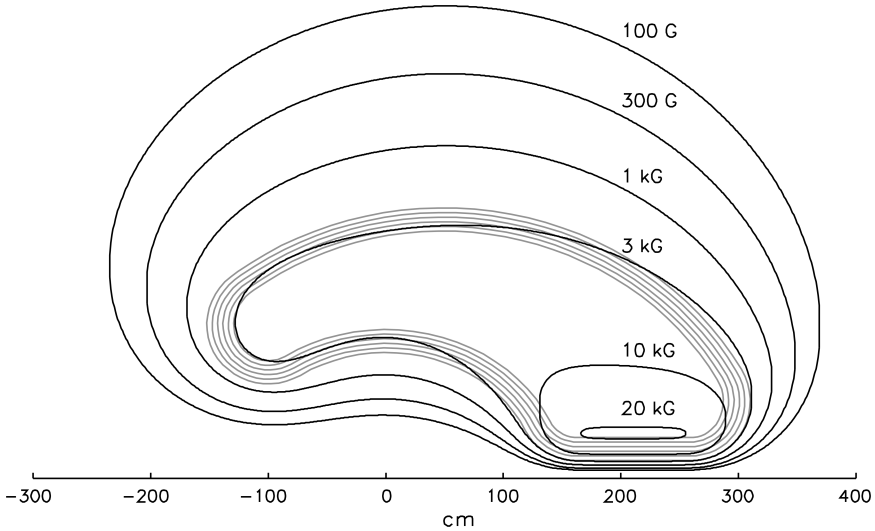

Figure 3.7: Profile of the strength of the CLAS magnetic field. Labelled field strengths are those found for maximum accepted current — approximately twice the current used for the FROST experiment.

the entire range of azimuthal angles (except for 2° cutouts between sectors), and polar angles from 7° to 145°. These scintillators were 3 mm thick and surrounded the target region in a hexagonal pattern, as shown in Figure 3.8. Time resolution for these detectors was approximately 280 ps.

A second array of scintillators and photomultiplier tubes, the time-of-flight array, was located in the outermost region of CLAS, as shown in Figure 3.6. In conjunction with the start counters and tracking, the time-of-flight system was used to associate the particle tracks within an event with the tagged photon for that event, and to measure the velocity associated with each track, which was necessary for particle identification, as discussed in section 4.1.2. The coverage in solid angle of the time-of-flight detector array was the same as that of the start counter array. These scintillators were 5.08 cm thick, approximately four meters long, and each scintillator subtended a polar scattering angle $\Delta\theta$ relative to the CLAS target of approximately 1.5°. Time resolution for each scintillator was approximately 100 ps.

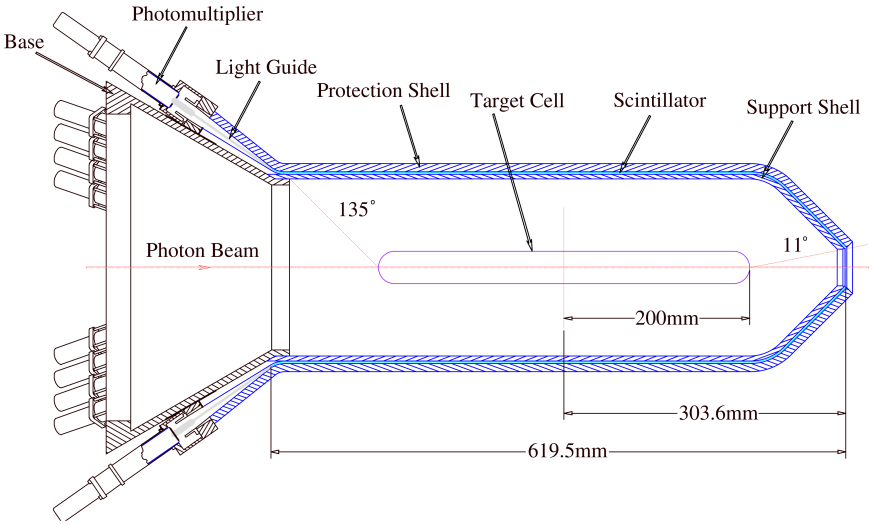

Figure 3.8: A cross section of the start counter, showing the component arrangements in two opposing sections. Photon beam enters from left.

3.4.2 Drift Chamber Subsystem [21, 24]

The six magnet coils divided the scattering solid angle into six independent sub-volumes called "sectors". Each sector was divided into three radial layers called "regions", each with its own drift chamber, as shown in Figure 3.6. In terms of the trajectory of a charged particle leaving the target and transiting CLAS, "Region One" was immediately outside the start counter discussed above, "Region Two" was between the coil cryostats, and "Region Three" was outside the magnet coils.

The radius of curvature R of a particle with electric charge q within the CLAS magnetic field B measures the momentum p of that particle through the relation $R = pe/qB$, where c is the speed of light.

The drift chambers were filled with an 88%:12% mixture of Ar and CO_2. A pump system cycled this gas with several complete volume exchanges per day. A feedback system ensured constant pressure within the drift chambers by dynamically adjusting the outflow rate in response to local atmospheric pressure fluctuations.

The drift chambers were filled with layers of field wires (held at a positive potential)

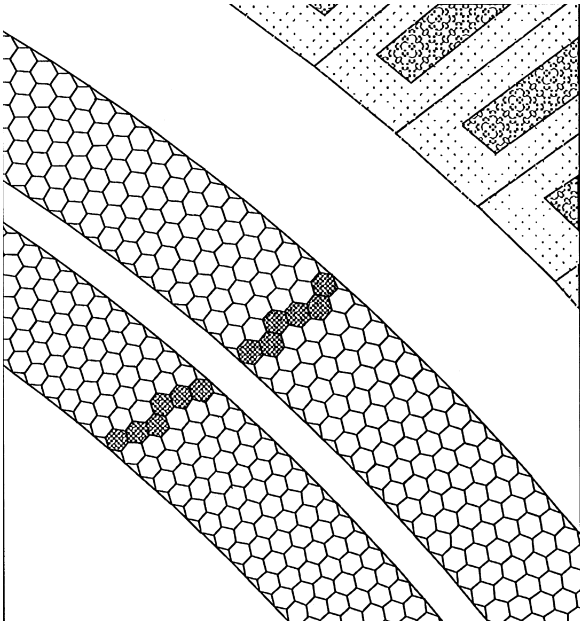

Figure 3.9: Diagram showing part of a drift chamber in Region Three. Hexagons are drawn to illustrate the boundaries of each cell formed by the six field wires which surround a sense wire at the center of each cell. The highlighted cells illustrate the track left by a charged particle.

and sense wires (held at a negative potential). Each sense wire was surrounded by six field wires, forming a hexagonal pattern. Toward the edges of the drift chambers, a layer of guard wires was arranged with voltages adjusted to approximate the field configuration of an infinite grid. In Region One, two groups held four sense wire layers each. In Regions Two and Three, two groups held six sense wire layers each. A diagram showing cross section of a portion of a drift chamber in Region Three is shown in Figure 3.9. In each chamber, the orientation of the second group was offset by six degrees to make azimuthal tracking possible. Altogether, the CLAS drift chambers contained over 35,000 sense wires. Typical inter-wire distances were on the order of 1 cm. Spatial resolution obtained for particle tracks was on the order of 300 μm.

Signals from each sense wire were preamplified in a single-channel differential amplifier located on the endplate of the drift chamber. These signals were then carried to a post-amplifier and discriminator board located in a crate in Hall B. This board produced

a digital output pulse which, in turn, was fed to a multi-hit, common-stop time-to-digital converter. The efficiency of detecting a charged particle passage was greater than 98%.

Ultimately, momentum measurement resolution for the drift chambers was $\sigma_p/p \approx 0.5\%$ in the forward polar scattering angle region ($\theta \lesssim 30^\circ$) and $\sigma_p/p \approx 1-2\%$ in the backward polar scattering angle region ($\theta \gtrsim 30^\circ$). Polar angle resolution was $\sigma_\theta \approx 1$ mrad and azimuthal angle resolution was $\sigma_\varphi \approx 4$ mrad.

3.5 The FROzen Spin Target (FROST)

The FROzen Spin Target (FROST) was a cryogenic target with polarized protons in the hydrogen constituents of a doped butanol mixture [18]. As shown in Figure 3.10, FROST was built as a series of concentric cylinders. Polarization was achieved with the dynamic nuclear polarization technique, described in section 2.6.

The primary target consisted of supercooled butanol (C_4H_9OH) beads doped with TEMPO ($C_9H_{18}NO$), a paramagnetic agent required for the dynamic nuclear polarization technique. The beads were produced by supercooling the butanol-TEMPO mixture in liquid nitrogen to produce beads of 1 to 2 mm diameter. A 5.1 T polarizing magnet was used to initially polarize the paramagnetic TEMPO radicals outside the CLAS detector. A microwave field then transferred spin from the TEMPO to the free nucleons within the butanol. These beads were loaded into a teflon target cup inside a helium dilution refrigerator, which maintained a temperature of approximately 30 mK to maintain the polarization over the course of many days, assisted by a holding magnetic field of approximately 0.50 T during data collection.

The holding magnet consisted of a pair of saddle-shaped four-layered coils of superconducting wire affixed to the outside of the 1 K heat shield of FROST. Current (35.5 A) was supplied to the holding magnet via a lead made of a combination of copper wire, superconducting ribbon, and NbTi wire.

The target polarization fraction was measured periodically using nuclear magnetic res-

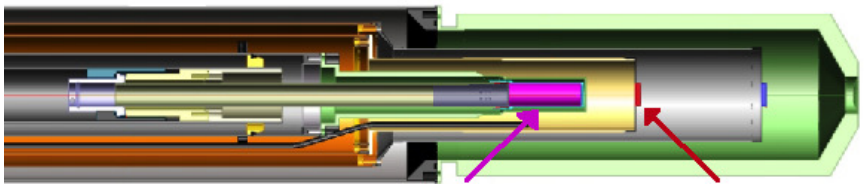

Figure 3.10: Cross section of the FROST target showing the location of the butanol material (magenta) and the carbon target (red). Also visible is a CH_2 target (blue) not used in this study. Surrounding the targets is the helium dilution refrigerator used to maintain the target at 30 mK. Not visible in this view is the holding magnet wound on the outside of the 1 K heat shield (grey). The dimensions of the butanol target are approximately 15 mm in diameter and 50 mm long. The entire target/cryostat assembly is approximately 2 m long — approximately 1/3 is shown here.

onance (NMR). The polarization fraction was typically $\approx 85\%$, with a relaxation rate of $\approx 1\%$ per day.

Downstream from the butanol target, a carbon target was attached to the end cap of the 1 K heat shield. This carbon target was used to estimate the unpolarized nuclear background in the butanol material and to provide a target for measuring the photon beam flux.

3.6 Data-acquisition System (DAQ) Trigger

The data acquisition system (DAQ) could process data at a rate of a few kHz, whereas the rate of scattering interactions within the target was on the order of 100 kHz. Event preselection was thus necessary in order not to swamp the DAQ. This preselection was accomplished by restricting event topologies and the range of incident photons. A two-layer trigger system was used, in which a "Level 1" trigger with no deadtime received prompt photomultiplier tube signals and was responsible for gating the electronics for the other detector electronics. The signals recorded by these detectors were then inspected by the "Level 2" trigger, which rejected event candidates without a correlated track in the drift chamber. The event preselection does not reduce the number of hadronic events seen. The Level 2 trigger simply ensures that a track is reasonable.

To be specific, for this experiment, the Level 1 trigger required sector-based coincidence

between the Start Counter and time-of-flight system in at least one sector in coincidence with the tagger, and the Level 2 trigger required a track candidate (hits in four out of six layers of the drift chambers) in the same sector as the Level 1 trigger. This trigger thus requires the detection of at least one charged particle in CLAS with momentum information.

3.7 Summary

The linearly-polarized electron beam was generated by CEBAF at Jefferson Lab. The electron beam was used to produce a beam of circularly-polarized photons. The energy of individual photons within this beam was measured indirectly using the Hall B photon tagger. The photon beam was incident on FROST, a cryogenic polarized target. The momenta and electric charge of decay products were measured in CLAS, a system of scintillators and drift chambers, which surrounded the target. The information from these pieces of apparatus permitted measurement of the polarization observables in this work, as described in the next chapter.

Chapter 4

DATA ANALYSIS

As derived in section 2.3, the η photoproduction process can be parameterized in terms of spin observables, including terms such as T and F, which modulate the azimuthal distribution of the unpolarized cross section, as given in equation 2.3, restated here for convenience:

$$\frac{d\sigma}{d\Omega} = \left(\frac{d\sigma}{d\Omega}\right)_0 \left(1 + P_t T \sin\varphi + P_t P_\gamma F \cos\varphi\right) . \tag{2.3}$$

The cross section is proportional to the number of η mesons produced per incident photon per target proton. Thus, in order to measure T and F, the following quantities must be known: the relative incident photon flux; the degrees of polarization of the target and incident photon beam; and the number of η mesons produced as a function of the kinematic variables center-of-mass energy W, azimuthal angle φ, and polar scattering angle $\theta_\eta^{\mathrm{cm}}$. This chapter examines the determination of these necessary quantities and the calculation of the measured observables.

The data analysis process can be outlined as follows:

- Identify the set of data runs containing usable data for analysis, omitting data runs where the various detector systems demonstrated problems or were determined to be of poor stability.

- Identify post-reaction charged-particle tracks in the drift chambers within the raw data.

- Apply energy-loss, momentum, and azimuthal-angle corrections.

- Determine the production vertex and initial 4-momentum vector for each track.

- Determine the angular offset of the orientation of the cryogenic target φ^{offset}, the photon flux, and the target and photon beam polarizations.

- Calculate the missing mass m_X assuming the reaction $\gamma p \to pX$ in order to identify η meson photoproduction events; sort the resulting spectra into kinematic bins based on the $\cos\theta_\eta^{\text{cm}}$, W, and φ.

- Within the missing-mass spectrum for each kinematical bin, remove backgrounds and obtain the η meson yield.

- Calculate T and F observables with a least-squares fit to the angular distribution of η production yields for the different polarization orientations.

4.1 Details of Technique

In the following sections, each of the steps mentioned in the introduction is discussed in detail.

4.1.1 Data Selection

The data used in this dissertation were collected during the g9b running period at Jefferson Lab, which began on March 18, 2010 and ended on August 12, 2010. This running period included data runs with both circularly- and with linearly-polarized photon beams incident on the transversely-polarized FROST target. (The linearly-polarized beam data were not needed for this analysis and will not be discussed further.) To be specific, the subset of the experimental data runs used in this analysis consists of g9b runs 62211–62704, collected from March 19 through April 19, 2010. The photon energies ranged from 20% (0.62 GeV) to 95% (2.93 GeV) of the 3.08173 GeV electron beam energy; however the analysis here is limited to photon energies 0.647 to 1.505 GeV because insufficient numbers of events exist at high photon energy from which to extract the polarization observables.

Some data runs had already been identified as bad in the data collection logs during data taking, typically due to incorrect or unstable experimental conditions. Additionally, some events were flagged within otherwise good data runs when photon polarization information was lost. All flagged data were excluded from this analysis. Finally, approximately 28% of the events recorded had two or more tagged photons within ± 1 ns of the vertex time. These multi-photon events were excluded because they do not result in an unambiguous kinematic reconstruction.

4.1.2 Particle Identification and Tracking Corrections

Particle identification was performed by the GPID algorithm [25], which is a time-based tracking reconstruction algorithm. The GPID algorithm uses momentum information for a scattered particle track measured by the drift chambers to calculate a theoretical β value for each possible particle identity for that track. These theoretical β values are compared to the measured value β_{m} obtained from the time-of-flight system and start counter for that track. The track is then assigned the identity which provides the closest match between the theoretical β and the measured β_{m} values. A time-walk correction [26] was applied to β_{m}. A second pass of the GPID algorithm [27, 28] was performed using the updated β_{m} value. Application of the time-walk correction and iteration of the GPID algorithm resulted in a significantly cleaner signal. A study to measure the influence of these corrections was performed for this work; although the percentage of protons which were reassigned was small ($\sim 2\%$), the corrections improve the quality of the spectra, particularly in high W bins where statistical uncertainties become relatively large [29, 30].

Once the particle type had been identified, several corrections were then applied. The 4-momentum of a particle as measured by the CLAS detector is not equal to the true initial 4-momentum for that particle because the particle loses some energy passing through the materials within the detector and target. This energy loss was estimated with the ELOSS

package [31], which contains a geometric model of the CLAS detector that specifies which type of material occupies each volume. In ELOSS, the measured trajectory of the particle is used to find the energy that would be lost in each volume of material intersected by the path of the particle. In this way, the initial 4-momentum of the tracked particle at the reaction point is calculated.

A further correction to the 4-momentum was required to correct a systematic shift in momentum as a function of detected azimuthal angle φ. Figure 4.1 shows the square of the missing mass m_x^2 calculated assuming the reaction $\gamma p \to \pi^+ X$, based on solely the π^+ information from CLAS and the incident photon energy. Without momentum corrections (top), the mass of the neutron is unphysically a function of the azimuthal angle φ. The effect of application of the momentum correction [32, 33] is shown on bottom, where the azimuthal dependence no longer appears.

4.1.3 Vertex Cuts

The default CLAS coordinate system sets the z-axis coaxial with the beam with the x-axis parallel to the laboratory floor in the plane normal to the beam [21]. To select particles originating from the butanol target, a cut was placed on the location of the vertex along the beamline such that the vertex position z was in the range -5.0 cm to 6.0 cm, where $z = 0$ corresponds to the center of the CLAS target region. The limits of this vertex cut were set based on the vertex for π meson tracks photoproduced with large transverse laboratory polar angle ($\theta_\pi^{\text{lab}} = 90 \pm 5^\circ$), as shown in Figure 4.2. The positions along the z-axis agree with the known locations of the targets. The widths are broader than the physical targets which gives an idea of the position resolution. Nevertheless, the peaks are sufficiently separated that target misidentification is not a concern.

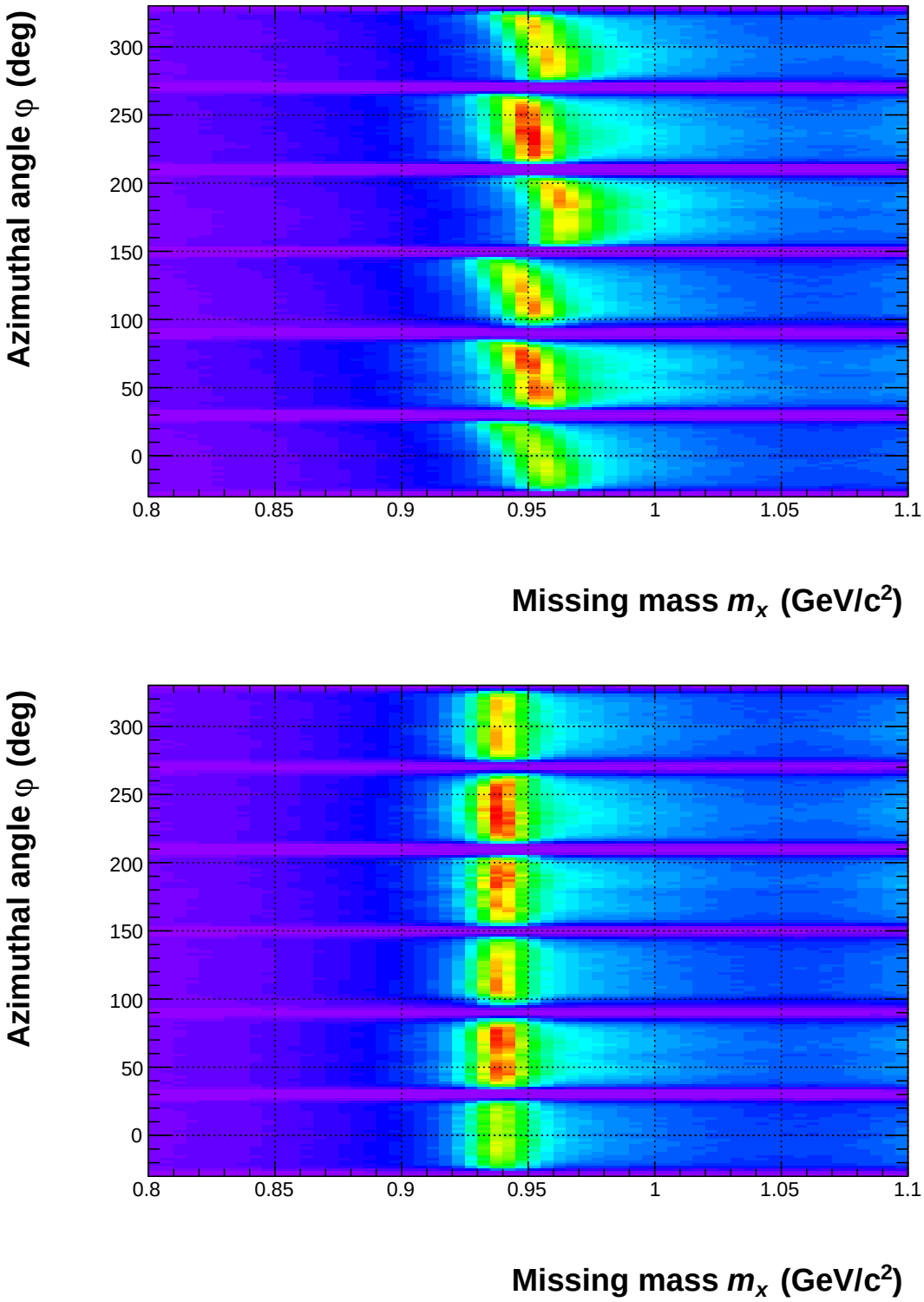

Figure 4.1: 2-d missing mass m_x vs azimuthal angle φ plots for all events in the full data set with one detected π^+ meson, assuming the reaction $\gamma p \to \pi^+ X$. Top: Without corrections, the neutron mass is unphysically a function of azimuthal angle. Bottom: The plot shown above demonstrates the effect of momentum corrections on the mass spectrum.

4.1.4 Missing Mass Technique and Kinematic Quantities

Since the electromagnetic calorimeter was not used in this work, the neutral η mesons could not be directly detected by CLAS because the remaining detector subsystems only see charged particles. Instead, η events were inferred from the decay products of the photoproduced η mesons by isolating events corresponding to η production from polarized protons. If an event only contained a detected recoil proton, an η event had to be identified using the missing mass technique, with $\gamma p \to pX$. The missing 4-momentum p_x^μ for each

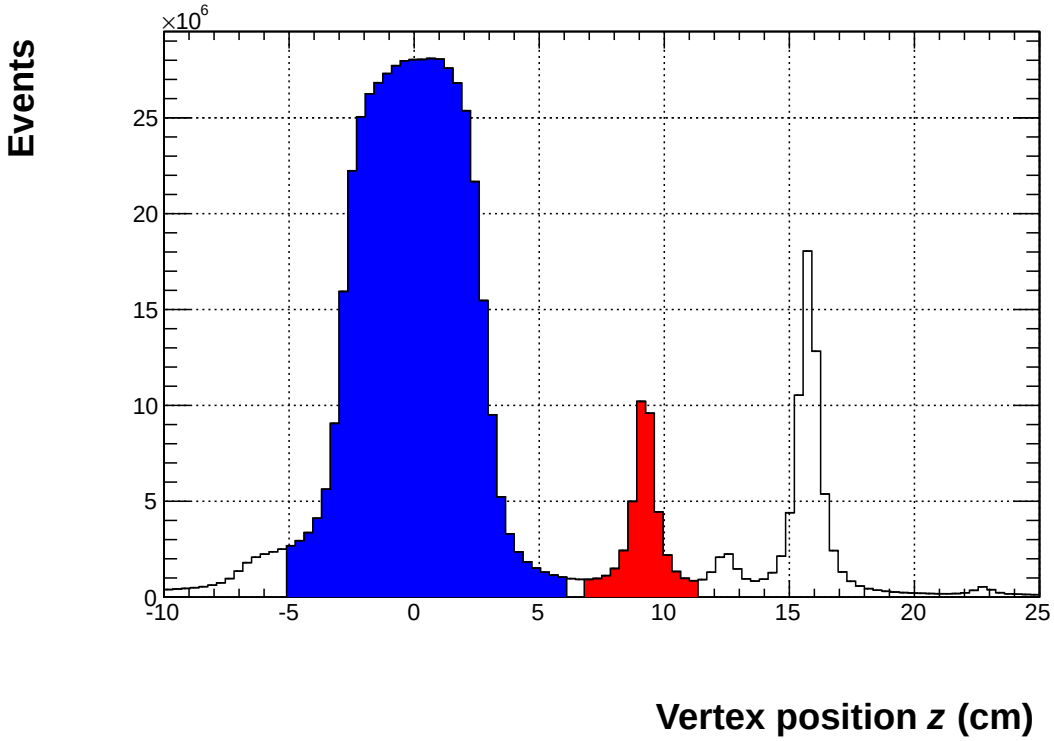

Figure 4.2: Distribution of vertex positions within the FROST target for all π^+ meson and proton tracks, demonstrating the separation of the targets. Shaded regions indicate the target cut regions. The blue region corresponds to the butanol target and the red region corresponds to the carbon target. The unshaded peaks correspond to an exit window and a CH_2 target which was not used for this dissertation.

particle track was calculated by

$$p_x^\mu = p_\gamma^\mu + p_i^\mu - p_f^\mu \,.$$

The missing mass m_x is the magnitude of the missing momentum 4-vector. Events were filled into histograms separately for different signs of target polarization P_t, photon beam polarization P_γ, $\cos\theta_\eta^{\rm cm}$, missing mass m_x, center-of-mass total energy W, and azimuthal angle φ. For each event, W was calculated using

$$W = \sqrt{m_p^2 + 2m_p c^2 E_\gamma}\,.$$

The value of $\cos\left(\theta_\eta^{\rm cm}\right)$ was taken from the center-of-mass frame 4-momentum vector p_x^μ.

4.1.5 Reaction Signature Cuts

When an η meson decayed via a charged mode and CLAS detected some or all of the decay products, an additional restriction was applied. The missing momentum p_y^μ was formed by subtracting the 4-vectors of all detected tracks from the initial 4-momentum:

$$p_y^\mu = p_\gamma^\mu + p_i^\mu - \sum_{\text{all final}} p^\mu \,.$$

To isolate η photoproduction events, the cuts on p_y^μ were applied, as given in Table 4.1. The resulting total integrated yields are shown in Figure 4.3.

4.1.6 Target Offset Angle φ^{offset}

Measurements of the azimuthal angle within CLAS are such that $\varphi = 0$ points parallel to the laboratory floor to the left side of the detector looking downstream ("beam left"). The direction of the target polarization orientation was determined experimentally. Asymme-

Table 4.1: The reaction signature cuts utilized when multiple charged tracks were detected. The windows were chosen to minimize the average propagated proportional uncertainty of background-subtracted η meson yield.

Reaction signature	Squared missing mass m_y^2 window $\left(\mathrm{MeV}^2/c^4\right)$
$\gamma p \to p\,\pi^+\pi^-\,(y)$	$9 \leq m_y^2 \leq 36$
$\gamma p \to p\,\pi^+\,(y)$	$45 \leq m_y^2 \leq 156$
$\gamma p \to p\,\pi^-\,(y)$	$45 \leq m_y^2 \leq 156$

try observables modulate the photoproduction yields with respect to this angle, so accurate determination of this direction is important. For this work, the direction of the target polarization was measured relative to the CLAS $\varphi_{\mathrm{CLAS}} = 0$ direction, defining a quantity called the target offset $\varphi_{\mathrm{CLAS}}^{\mathrm{offset}}$. To find $\varphi_{\mathrm{CLAS}}^{\mathrm{offset}}$, events were binned as a function of the azimuthal angle φ, and the quantity $A \sin\varphi$ was extracted at each angle, where $A = P_{\mathrm{P}}\,T$. Figure 4.4 demonstrates a fit within one kinematic bin. The amplitude of the resulting sin function is the target asymmetry, but the parameter of interest for determining the target offset is the phase $\varphi_{\mathrm{CLAS}}^{\mathrm{offset}}$. A "coarse adjustment" of -60° had already been applied to the raw azimuthal angle, so, for the bin shown, the phase fit parameter yielded approximately -3.4° for a total offset angle of -63.4°. The reaction $\gamma p \to p\,\pi^+$ was chosen since that reaction has a large cross section and relatively low background. Within each $\cos(\theta_\pi^{\mathrm{cm}})$, W bin, each yield asymmetry was fit to the function $A \sin\left(\varphi_{\mathrm{CLAS}} - \varphi_{\mathrm{CLAS}}^{\mathrm{offset}}\right)$. The best fit for $\varphi_{\mathrm{CLAS}}^{\mathrm{offset}}$ was found to be $-62.9 \pm 0.3^\circ$. In the analyses reported for η measurements, the angle φ used to fit yields is the azimuthal angle $\varphi_{\mathrm{CLAS}}^{\eta}$ of the meson minus the offset angle $\varphi_{\mathrm{CLAS}}^{\mathrm{offset}}$. That is, $\varphi = \varphi_{\mathrm{CLAS}}^{\eta} - \varphi_{\mathrm{CLAS}}^{\mathrm{offset}}$.

4.1.7 Photon Flux N_γ

For each polarization orientation of the target and W bin, the photon flux must be measured in order to determine an asymmetry observable. This photon flux was not directly

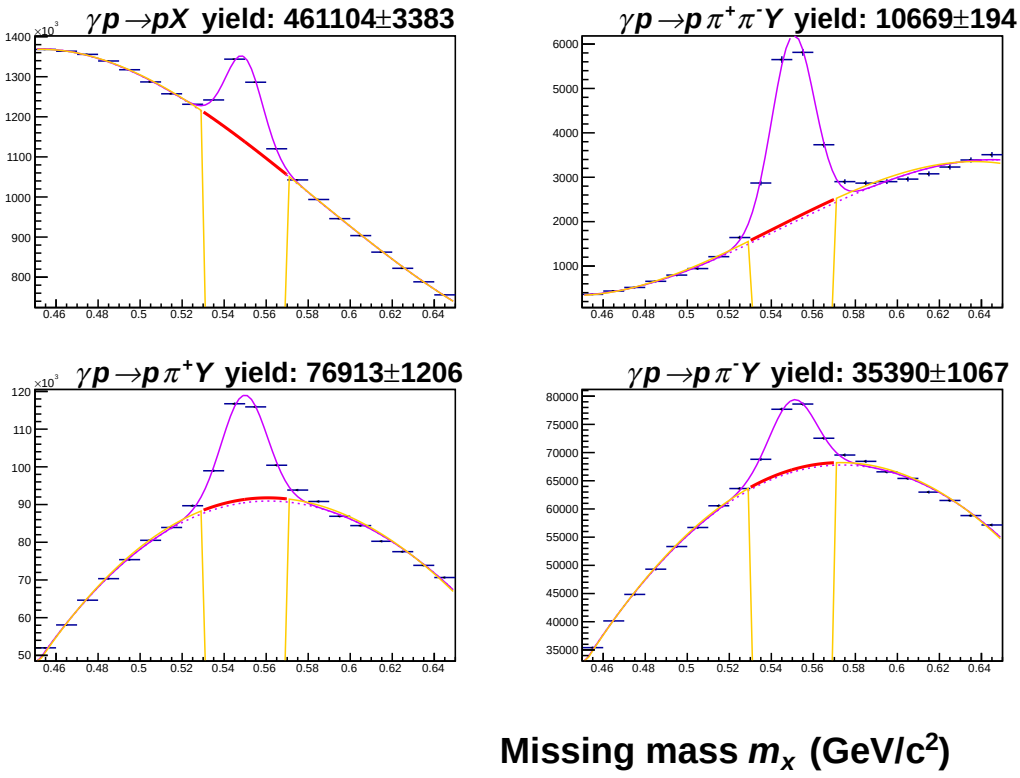

Figure 4.3: The missing mass m_x spectrum for all data in all kinematic bins for each reaction signature indicated in Table 4.1. The curves shown are third-order polynomial backgrounds added to gaussian peaks to estimate the total η meson yield for each reaction channel.

measured, so a proportional quantity was sought. An event was included in the flux measurement if the event had the reaction signature $\gamma p \to pX$ or $\gamma p \to \pi^+ X$ and the production vertex was within the carbon target (7.0 cm to 11.0 cm). The uncertainty of this relative normalization measurement was taken to be the Poisson uncertainty, $\sigma_N = \sqrt{N}$.

4.1.8 Target Polarization Fraction P_t

The average target polarization fraction P_t for each target orientation is required to determine T and F. The target polarization fraction was monitored during the g9b running period and stored in a file which contained a measurement for each run. Because the target polarization fraction was measured on a run-by-run basis, the average target polarization fraction is the average of the measured value for each particular run, weighted by the num-

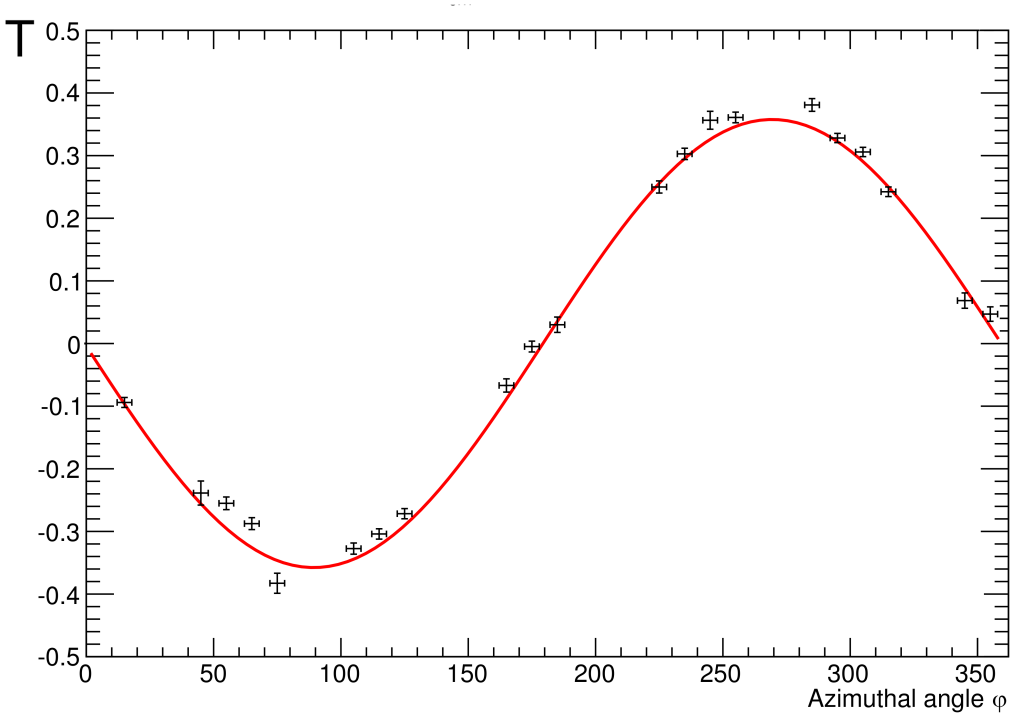

Figure 4.4: Example fit used to obtain target offset angle for $W = 1.500 \pm 0.025$ GeV, $\cos\theta_\pi^{\rm cm} = 0.75 \pm 0.25$ for the target offset study. The fit equation is $y(\varphi_{\rm CLAS}) = A\sin\left(\varphi_{\rm CLAS} - \varphi_{\rm CLAS}^{\rm offset}\right)$.

ber of events in that run. That is, for a given W and target orientation, the average target polarization P_t was determined from

$$P_t = \frac{\sum N_i P_{t,i}}{\sum N_i},$$

where $P_{t,i}$ is the measured target polarization fraction of the $i^{\rm th}$ run, and N_i is the number of $\gamma p \to \pi^+(n)$ events from the carbon target with this polarization fraction in the $i^{\rm th}$ run. The uncertainty of this quantity was taken to be

$$\sigma_{P_{\rm t}} = \sqrt{\sum \left(\frac{\partial P_{\rm t}}{\partial P_{{\rm t},i}}\right)^2 \sigma^2_{P_{{\rm t},i}} + \left(\frac{\partial P_{\rm t}}{\partial N_i}\right)^2 \sigma^2_{N_i}}$$
$$= \sqrt{\sum \left(\frac{N_i}{N}\right)^2 \sigma^2_{P_{{\rm t},i}} + \left(\frac{P_{{\rm t},i} - P_{\rm t}}{N}\right)^2 \sigma^2_{N_i}},$$

where $\sigma_{P_{t,i}}$ is the uncertainty in the measured target polarization fraction of the $i^{\rm th}$ run, and σ_{N_i} is the Poisson uncertainty due to the finite sample size for the weighting factor N_i. In this expression, the quantity σ_{N_i} is negligible compared to the first term. Thus, $\sigma_{P_{\rm t}}$ is simply

$$\sigma_{P_{\rm t}} \approx \sqrt{\sum \left(\frac{N_i}{N}\right)^2 \sigma^2_{P_{{\rm t},i}}}.$$

The distribution of target polarization values is shown in Figure 4.5. Typical target polarization values were approximately $\pm 80\%$. While this figure shows average positive and negative target polarization values, data from each run were analyzed using the measured target polarization for that run.

4.1.9 Photon Beam Polarization

The average photon beam polarization P_γ for each target and photon beam orientation and W bin is required to determine F. For circularly polarized photons, the photon beam polarization can be calculated from the measured photon energy E_γ, the incident electron beam energy E_e, and the linear polarization of the incident electron beam P_e. As discussed in section 2.4, the photon beam polarization is given by Equation 2.5, restated here for convenience:

$$P_\gamma = P_e \frac{4\tilde{E} - \tilde{E}^2}{4 - 4\tilde{E} + 3\tilde{E}^2}, \tag{2.5}$$

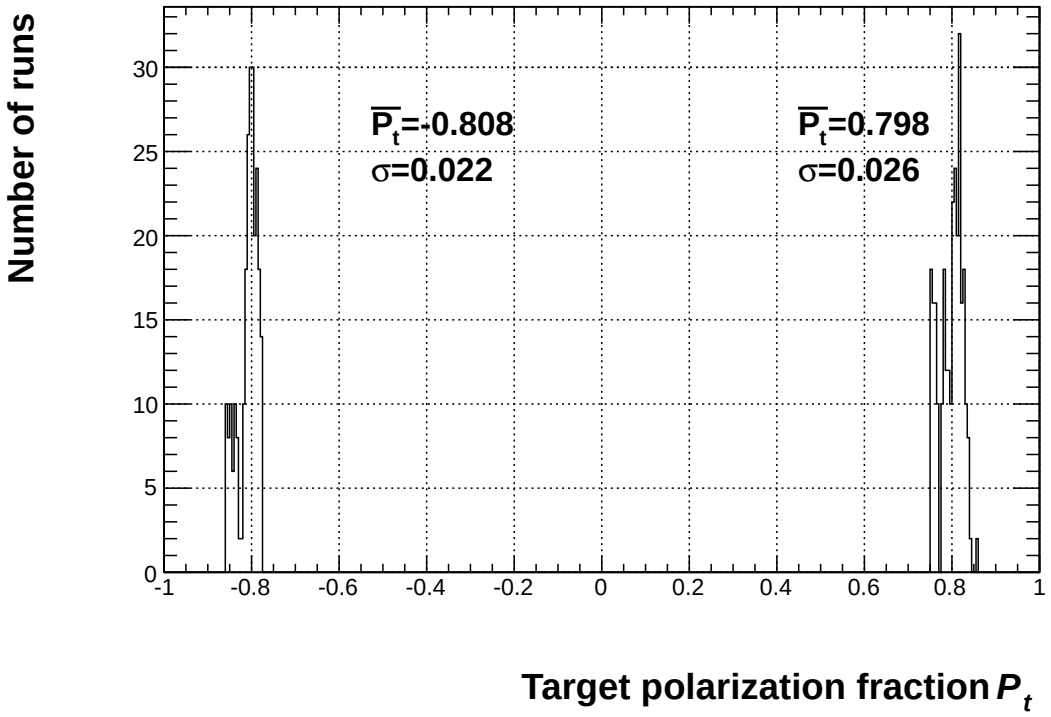

Figure 4.5: Distribution of target polarization fractions for runs used in this work. The left-hand peak indicates the average polarization fraction for the 'negative' target orientation, and the right-hand peak indicates the average polarization fraction for the 'positive' target orientation.

where, for this experiment, $\tilde{E} = \frac{E_\gamma}{E_e}$ is the ratio of the emitted photon energy E_γ to the incident electron energy E_e, P_e was the electron beam linear polarization, and $E_e = 3.08173$ GeV was the incident electron energy. The average photon beam polarization fraction is the simple average of all measured photon beam polarizations for that W and orientation of target and photon beam. As with the determination of P_t, only events from the carbon target with reaction signature $\gamma p \to \pi^+ X$ were used to determine P_γ. The uncertainty of the photon-beam polarization is dominated by the uncertainty of the electron-beam polarization, which was approximately 1.5%. The polarization of the electron beam was measured with a Møller polarimeter, as described in section 3.2. Since Møller measurements were taken intermittently, the electron beam polarization was taken from the most recent such measurement. As with the target-polarization fraction, the uncertainty is dominated by the

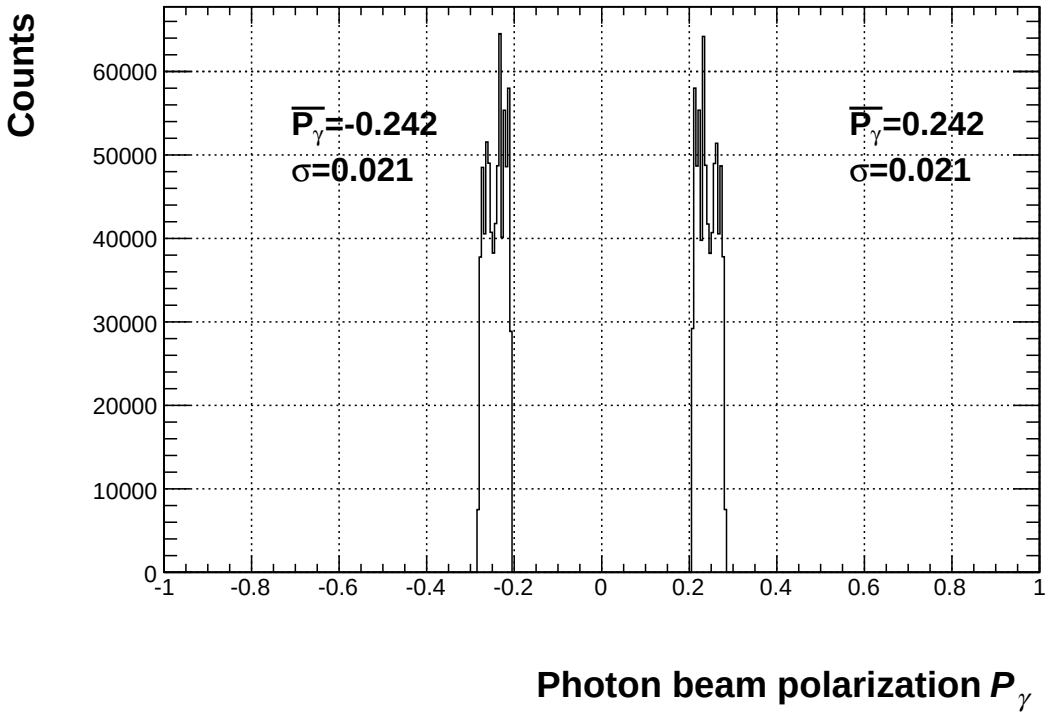

Figure 4.6: Distribution of photon beam polarizations for runs used in this work for the $W = 1.55$ GeV bin and positive target polarization orientation. The left-hand peak indicates the average polarization for the 'negative' photon-beam orientation and the right-hand peak indicates the average polarization for the 'positive' photon-beam orientation. The width of each distribution (labelled as σ) is not the uncertainty used — see text.

uncertainty of each measurement, so the Poisson-counting uncertainty term was neglected from the error propagation.

As an example, the distribution of photon-beam polarizations for the 'positive' target orientation and $W = 1.55$ GeV is shown in Figure 4.6. As with the distribution of target polarization fractions, the mean value and width shown on the figure indicate the variation of photon beam polarization values within the data set.

4.1.10 Yield Extraction

A method was developed to extract η yields as accurately as possible from the presence of multi-pion and bound-nucleon background, taking detector efficiencies into ac-

count. The kinematic cutoff at energies near the photon-energy threshold for η meson photoproduction results in a background 'shoulder', complicating background subtraction. For example, in the $W = 1.55\,\mathrm{GeV}$ bin, the entire η yield peak lies within this shoulder region, so the background fit range was $m_X = 480\,\mathrm{MeV/c^2}$ to $610\,\mathrm{MeV/c^2}$. For the $W = 1.60\,\mathrm{GeV}$ bin, the background fit range was $m_X = 450\,\mathrm{MeV/c^2}$ to $610\,\mathrm{MeV/c^2}$. An example missing-mass plot for the latter energy is shown in Figure 4.7. The shoulder begins at approximately $570\,\mathrm{MeV/c^2}$ so the background fit range was limited at the positive end. Without this limitation, the polynomial background function would misbehave under the peak region, typically resulting in over-subtraction and subsequent suppression of asymmetries. The red line shows the polynomial part of the full fit equation (shown in magenta) over the mass range where integration is performed. This range is chosen to minimize proportional uncertainty as discussed below. For all higher-energy bins, the background fit range was $m_X = 450\,\mathrm{MeV/c^2}$ to $650\,\mathrm{MeV/c^2}$.

The fit function used a third-order polynomial background added to a gaussian peak:

$$y(x) = c_0 + c_1(x-c_5) + \frac{1}{2}c_2(x-c_5)^2 + \frac{1}{6}c_3(x-c_5)^3 + c_4 \exp\left(-\frac{(x-c_5)^2}{2c_6^2}\right).$$

The centroid of the peak in this fit function is given by c_5. The polynomial terms are written in the form $c_n\frac{(x-\bar{x})^n}{n!}$, so that each coefficient reflects the mean, slope, curvature, etc. of the background at the center of the peak. This form for the fit was chosen to maximize intelligibility of each term during analysis.

In order to find seed values for the fitting routine, the histogram was sampled at three places: $533\,\mathrm{MeV/c^2}$ and $563\,\mathrm{MeV/c^2}$ to estimate the background part and $548\,\mathrm{MeV/c^2}$ to estimate the amplitude of the gaussian part. Specifically, the parameters were seeded with the values given in Table 4.2.

The final η yield for each kinematic bin was found by subtracting the integral of the

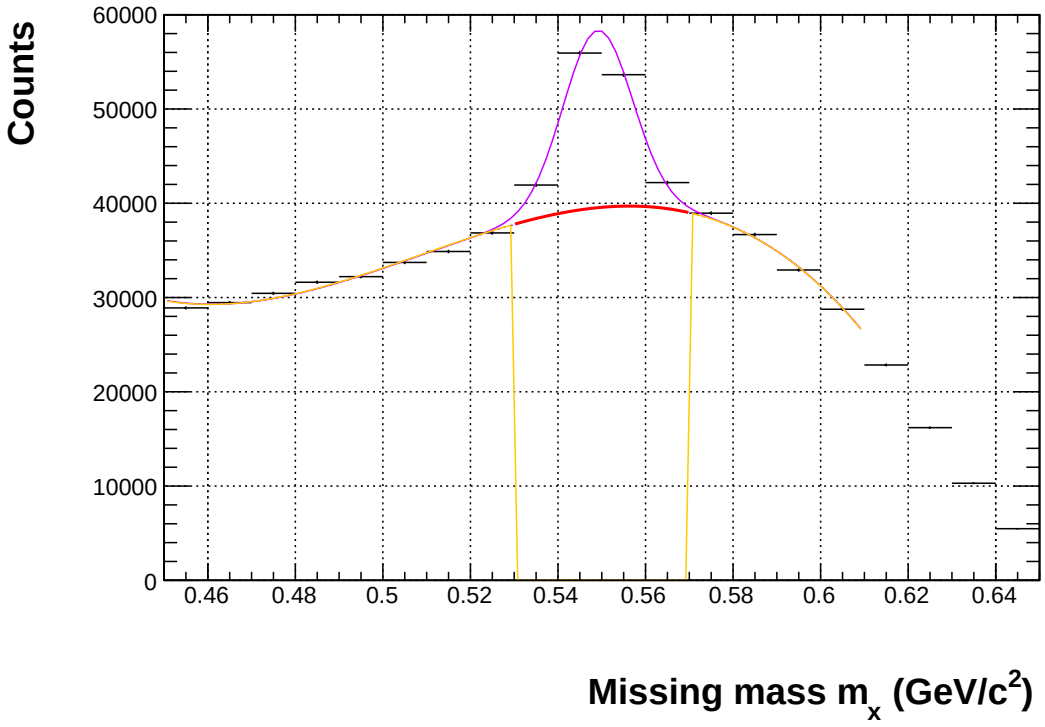

Figure 4.7: An example missing-mass plot demonstrating a kinematic shoulder beginning just beyond the η meson peak, around 0.570 GeV. This effect complicates background subtraction. This plot is the sum of all azimuthal angles and beam and target polarization orientations for the kinematic bin with $W = 1.60$ GeV and $\cos\theta_\eta^{\mathrm{cm}} = -0.75$.

polynomial part of the fit in the region containing the η peak from the total number of counts in the same region of the histogram. The uncertainty of the η yield was calculated from the covariance matrix returned by the fitting routine and the Poisson uncertainty, thusly:

$$Y_\eta = Y_{\mathtt{tot}} - Y_{\mathrm{bg}} \pm \sqrt{\sigma_{\mathtt{tot}}^2 + \sigma_{\mathrm{bg}}^2},$$

where $Y_{\mathtt{tot}}$ was the sum of the counts in the fit region of the kinematic bin, Y_{bg} was the integral of the polynomial part of the background in the fit region, $\sigma_{\mathtt{tot}}^2$ was the Poisson uncertainty (which is the total counts Y_{tot} in the region) and σ_{bg}^2 was obtained from the covariance matrix of the polynomial terms in the fit. The integration region was determined separately for each kinematic bin by finding the range about the peak which minimized

Table 4.2: Initial seeds for fit function where y_m indicates the contents of the histogram bin with mass m.

Parameter	Seed	Minimum	Maximum
c_0	$\frac{y_{533}+y_{563}}{2}$	0	$10 \times$ seed value
c_1	$\frac{y_{563}-y_{533}}{30\ \mathrm{MeV/c^2}}$	0	$10 \times$ seed value
c_2	0	No limit	No limit
c_3	0	No limit	No limit
c_4	$y_{548} - \frac{y_{533}+y_{563}}{2}$	$\frac{1}{10} \times$ seed value	$4 \times$ seed value
c_5	$548\ \mathrm{MeV/c^2}$	$530\ \mathrm{MeV/c^2}$	$570\ \mathrm{MeV/c^2}$
c_6	$10\ \mathrm{MeV/c^2}$	$5\ \mathrm{MeV/c^2}$	$25\ \mathrm{MeV/c^2}$

the average proportional uncertainty. The closed-form expression for such an integration range is extremely unwieldy. A first-order approximation to the uncertainty-minimizing expression was found to be

$$\hat{N} = 1.80 - 0.27 \cdot \texttt{SNR},$$

where $\hat{N}$ is the number of standard deviations about the peak and SNR is the average signal-to-noise ratio for all events in the same kinematic bin. The complete set of background fits are viewable online [34].

4.1.11 Extracting Observables

The T and F observables are obtained from data runs with a circularly-polarized photon beam incident on a transversely-polarized target as given in equations 2.3 and 2.4, restated here for convenience:

$$\frac{d\sigma}{d\Omega} = \left(\frac{d\sigma}{d\Omega}\right)_0 \left(1 + P_t T \sin\varphi + P_t P_\gamma F \cos\varphi\right). \tag{2.3}$$

$$\frac{d\sigma}{d\Omega} = \frac{Y_\eta}{N_\gamma \rho L \varepsilon}. \tag{2.4}$$

The measured spectra have significant background contributions. An event with reaction signature $\gamma p \to pX$ might arise from the production of an η meson from a free proton (the desired type of event) or the proton track could be, for example, due to a proton which inelastically scattered from a carbon or oxygen nucleus or a scattering involving some process other than $\gamma p \to p\,(\eta)$ production (background events). When the missing mass is reconstructed, free nucleon η production events produce a peak at the known η meson mass of $547\,\mathrm{MeV/c^2}$. The background about that peak arises from other reactions and bound nucleon processes, which may have their own asymmetries.

This background must be subtracted for an accurate measurement of observables. Combining equations 2.3 with 2.4 and adding background terms, the observed yield is

$$\begin{aligned} Y_i = {} & N_{\gamma,i}\left(Y_{\eta,\mathrm{unpol}} + f_{\mathrm{bg},1}\right) \\ & + N_{\gamma,i}P_{\mathrm{t},i}\left(Y_{\eta,\mathrm{unpol}}\,T\,\sin\varphi + f_{\mathrm{bg},2}\right) \\ & + N_{\gamma,i}P_{\mathrm{t},i}P_{\gamma,i}\left(Y_{\eta,\mathrm{unpol}}\,F\,\cos\varphi + f_{\mathrm{bg},3}\right), \end{aligned}$$

where $Y_{\mathrm{unpol}} = \rho\,L\,\varepsilon\,\frac{d\sigma}{d\Omega}_0 R$ is the equivalent 'unpolarized' yield, R is the sum of the branching ratios for the detected η decay branches, and f_{bg} are unknown functions which encompass the physics of the unwanted background terms and branches other than $\eta \to p$ neutrals or $\eta \to p\,\pi^+\pi^-\pi^0$. The index i denotes the four possible combinations of target and beam polarizations, as shown in Table 4.3. Peak extraction removes the background terms, and the following expression results:

$$Y_{\eta,i} = N_{\gamma,i}Y_{\eta,\mathrm{unpol}} + N_{\gamma,i}P_{\mathrm{t},i}Y_{\eta,\mathrm{unpol}}\,T\,\sin\varphi + N_{\gamma,i}P_{\mathrm{t},i}P_{\gamma,i}Y_{\eta,\mathrm{unpol}}\,F\,\cos\varphi\,. \qquad (4.1)$$

Usually, an asymmetry is extracted for each φ bin so that efficiency terms cancel when calculating the asymmetry. However, performing the extraction for each φ bin separately

is not the only approach that can be taken. In this section, a method of extracting the T and F observables is described which takes into account all φ bins simultaneously.

Before extracting T and F, detector efficiencies must be accounted for. As long as at least three of the four combinations indicated in Table 4.3 succeed for a particular azimuthal bin, $Y_{\eta,\text{unpol}}$ can be extracted. For each combination i, Equation 4.1 is of the form $y(\mathbf{x}) = \sum_j c_j x_j$, where $x_1 = N_\gamma$, $x_2 = N_\gamma P_t \sin\varphi$, and $x_3 = N_\gamma P_t P_\gamma \cos\varphi$ and $c_1 = Y_{\eta,\text{unpol}}$, $c_2 = Y_{\eta,\text{unpol}} T$, and $c_3 = Y_{\eta,\text{unpol}} F$. We can write

$$\begin{pmatrix} \sum_i x_1 y \\ \sum_i x_2 y \\ \sum_i x_3 y \end{pmatrix} = \begin{pmatrix} \sum_i x_1^2 & \sum_i x_1 x_2 & \sum_i x_1 x_3 \\ \sum_i x_1 x_2 & \sum_i x_2^2 & \sum_i x_2 x_3 \\ \sum_i x_1 x_3 & \sum_i x_2 x_3 & \sum_i x_3^2 \end{pmatrix} \cdot \begin{pmatrix} c_1 \\ c_2 \\ c_3 \end{pmatrix}$$

or

$$\mathbf{b} = A\,\mathbf{c}$$

and solve for the vector of parameters with matrix methods, giving $\mathbf{c} = A^{-1}\mathbf{b}$. Each yield $Y_{\eta,i}$ in the entire data set is then divided by the extracted $Y_{\eta,\text{unpol}}$ for the same azimuthal bin. Since $Y_{\eta,\text{unpol}}$ comes from a sum over $Y_{\eta,i}$, the uncertainty in $\frac{Y_{\eta,i}}{Y_{\eta,\text{unpol}}}$ has a nonvanishing covariance term. The covariance expressions become very unwieldy. To correctly handle the covariance calculations, a Python package called "uncertainties" was used to track all error propagation steps, including calculating the covariance between related terms.

Once $Y_{\eta,\text{unpol}}$ was determined for each azimuthal bin, each $Y_{\eta,i}$ was divided by $Y_{\eta,\text{unpol}}$, which cancels the detector efficiency terms so that data from all angles could be used simultaneously and the observables extracted. As a second benefit, this method made simultaneous extraction of T and F possible with matrix methods. Here, the sums must be weighted by the inverse of the variance: $\sum_i x_i \to \sum_i \frac{1}{\sigma_i^2} x_i$. The expression $\sigma_i = \sqrt{\sigma_{y_i}^2 + \sum_j \left(\frac{dy}{dc_j}\right)^2 \sigma_{c_j}^2}$

Table 4.3: The four possible combinations of orientations of photon beam (P_γ) and target (P_t) polarizations. These are labeled by the index i.

i	sign(P_t)	sign(P_γ)
0	$-$	$-$
1	$-$	$+$
2	$+$	$-$
3	$+$	$+$

is needed to account for the uncertainties in the dependent parameters since these uncertainties are non-negligible. The terms $\frac{dy}{dc_j}$ in turn depend on T and F, so an iterative approach is required in order to obtain the correct covariance matrix. An existing software library, SciPy, was used to solve this equation [35].

Chapter 5

RESULTS

The previous chapters explained the technique used to extract the asymmetries T and F. In this chapter, these results are shown and compared to theoretical predictions. The measurements span an energy range from $W = 1.550\,\text{GeV}$ to $W = 1.800\,\text{GeV}$ with bin widths of 50 MeV are polar angle bins given by $\cos\theta_\eta^{\text{cm}} = 0.75$, -0.45, -0.15, and 0.15 with a bin width of 0.3. This kinematic range overlaps a recent experiment [36]. Where possible, asymmetry observables are compared to results from that experiment. The ETA-MAID model is presented here as one example of a theoretical model that will benefit from inclusion of the results shown here.

5.1 ETA-MAID Model

The Mainz Unitary Isobar Model (MAID) is a group of models for describing scattering data in terms of nucleon resonances [37]. ETA-MAID is the particular model that predicts resonances involved in η-meson processes. The principal assumptions made by this model are that resonances have a Breit-Wigner given by a probability density function for each resonance j

$$f(E) = \frac{k_j}{\left(E^2 - M_j^2\right)^2 + \left(M_j\,\Gamma_j\right)^2}\,. \tag{5.1}$$

where k_j is a proportionality constant, E is the production energy, M_j is the rest mass of the resonance, and Γ_j is the decay width of the resonance. The model also includes a unitarization factor of $e^{i\,\phi_j}$ which is chosen such that the total phase of the multipole is equal to the observed phase shift δ as given by the equation $\Sigma_j\,\phi_j = \delta$. Finally, ETA-MAID includes non-resonant processes with an effective Lagrangian approach. The theory curves

shown in subsequent sections are for the 2002 ETA-MAID model. New results have been shown by the ETA-MAID group in conference proceedings but are not yet available.

5.2 Observables T and F

Current preliminary results for the reaction $\gamma p \to p(\eta)$ are presented below, along with phenomenological fits from Bonn [38], MAID, and SAID [39] and data points from the existing world data set. Figure 5.1 shows T asymmetries for η meson photoproduction as a function of polar angle measure for each center-of-mass energy bin. Figure 5.2 shows F double-polarization asymmetries for η meson photoproduction as a function of polar angle measure for each center-of-mass energy bin.

Prior measurements are available for comparison: an experiment performed in Bonn published in 1998 (labeled BONN-98) gave low-energy data for T and an experiment performed in Mainz published in 2014 (labeled MAIN-14) [40, 36]. The results of this dissertation form a "tie-breaker" where these experiments had different results — in every such case, the results of this dissertation support the MAIN-14 data.

5.3 Excitation Plots

A projection of the observable data onto the other kinematic axis shows observables as a function of center-of-mass energy for each polar angle bin. Figure 5.3 presents the data for T in this format and Figure 5.4 presents the data for F in this format.

Note that the statistical limitations of the CLAS data restricted the polar angle resolution. Therefore, the $\cos\left(\theta^{\eta}_{\mathrm{cm}}\right)$ bins shown in these figures (ie, -0.75, -0.45, -0.15, 0.15) are not the same as for BONN-98 or MAIN-14. Where data vary quickly with polar angle, this

may exaggerate apparent differences. For example, at 1.55 GeV: BONN-98 reported that $T = 0.052 \pm 0.040$ at $\cos\left(\theta_{\mathrm{cm}}^{\eta}\right) = -0.819$, where MAIN-14 measured $T = 0.153 \pm 0.017$ at $\cos\left(\theta_{\mathrm{cm}}^{\eta}\right) = -0.750$, an apparent difference of $\Delta T = 0.101 \pm 0.043$ or 2.5σ over the BONN-98 measurement. However, a linear interpretation the MAIN-14 data from a nearby bin suggests at the BONN-98 polar angle, MAIN would observe $T = 0.121 \pm 0.013$, a difference of $\Delta T = 0.070 \pm 0.042$ or 1.7σ.

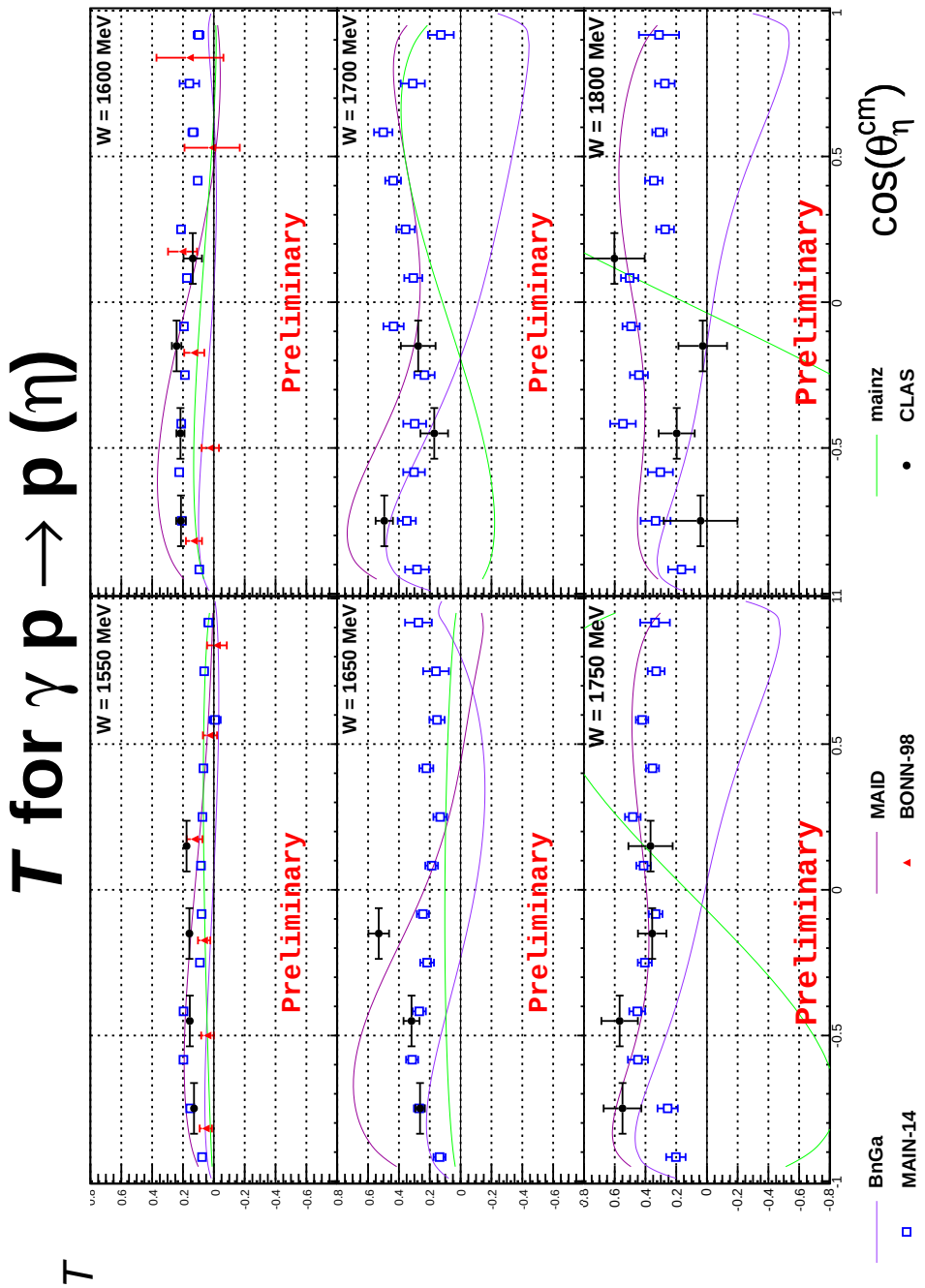

Figure 5.1: The T observable versus $\cos\left(\theta^{\eta}_{\mathrm{cm}}\right)$ for the process $\gamma p \to p\,(\eta)$ for center-of-mass energies W from 1550 MeV through 1800 MeV.

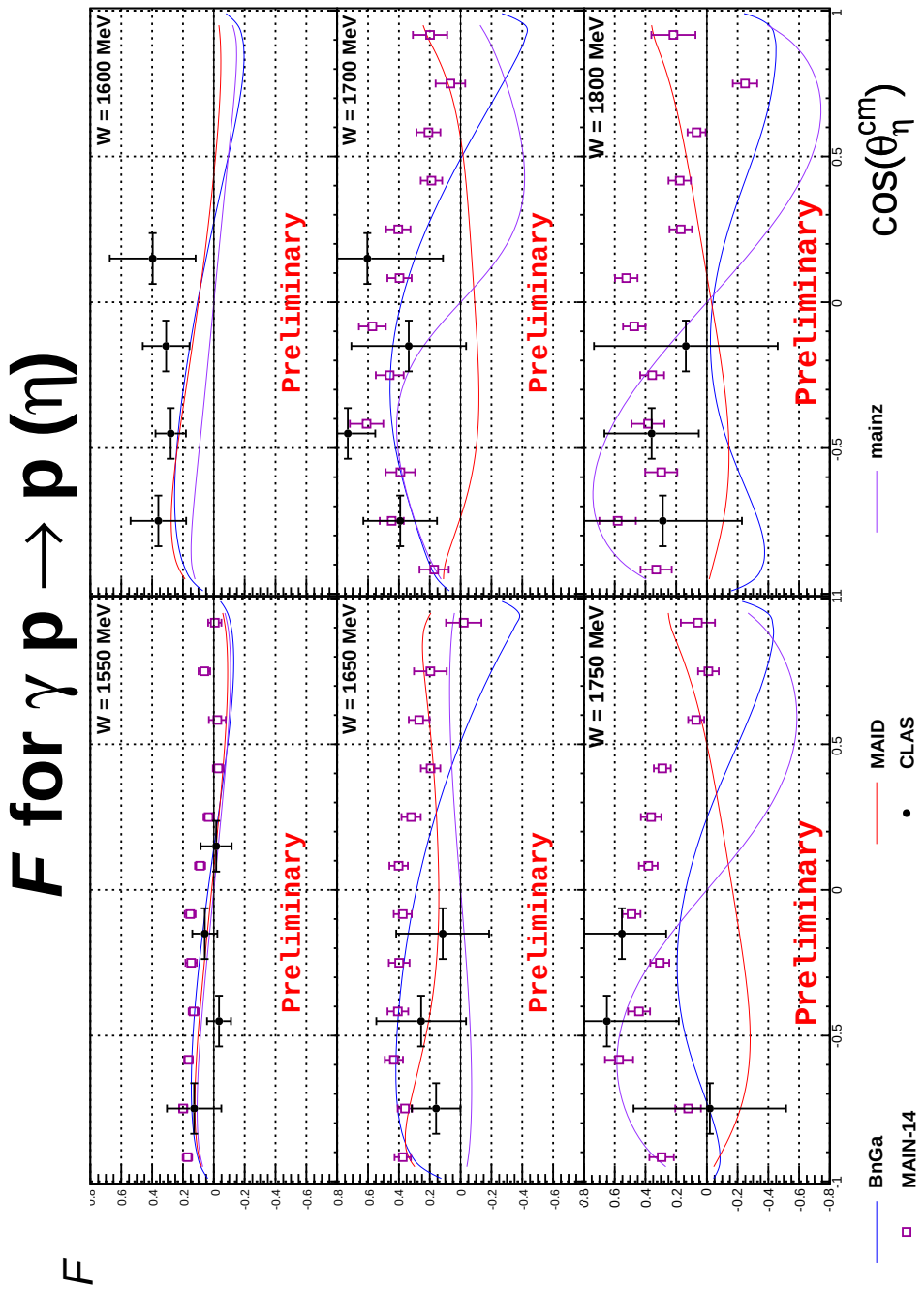

Figure 5.2: The F observable versus $\cos\left(\theta_{\mathrm{cm}}^{\eta}\right)$ for the process $\gamma p \to p\,(\eta)$ for center-of-mass energies W from1550 MeV through 1800 MeV.

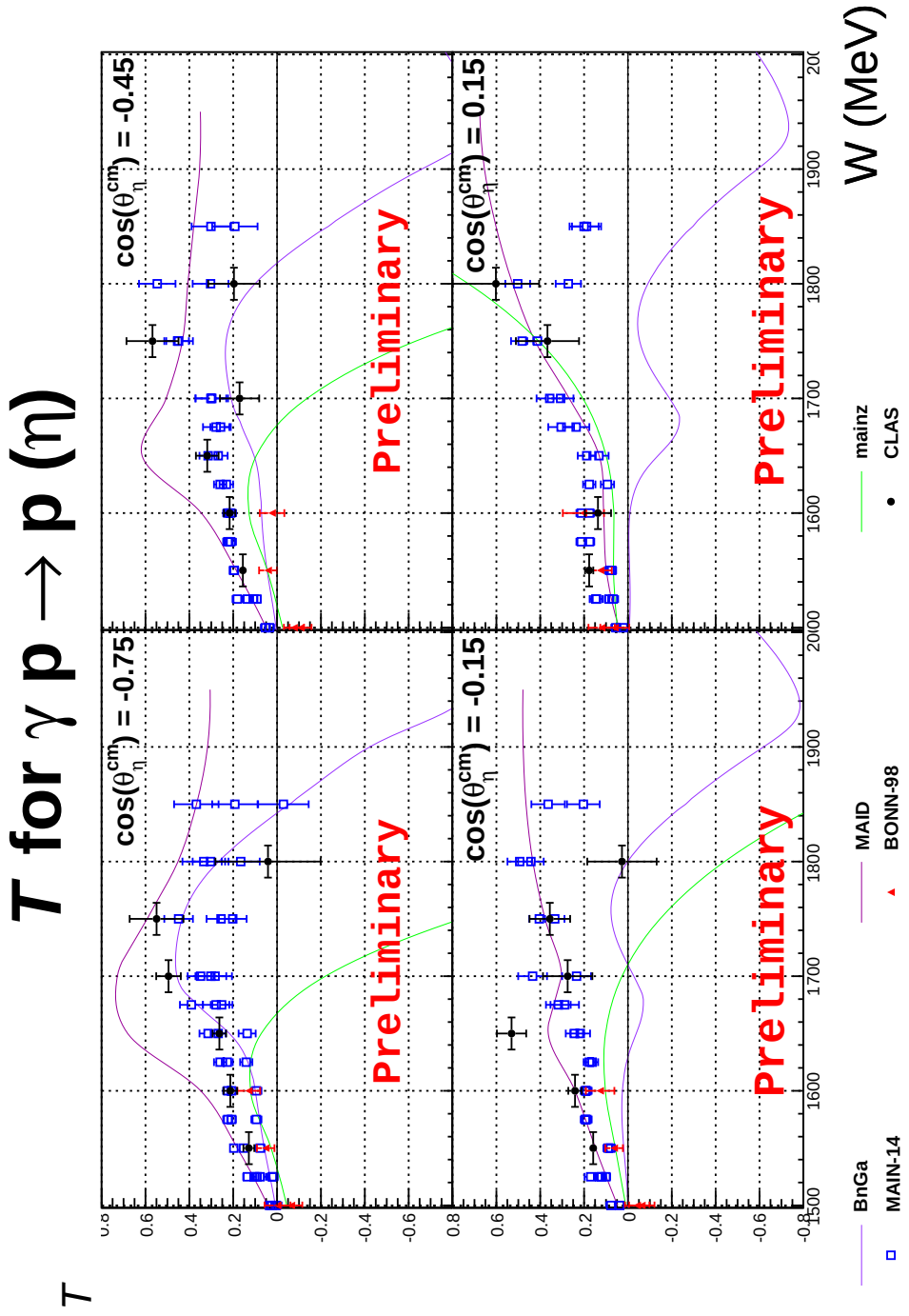

Figure 5.3: The T observable versus W for the process $\gamma p \to p(\eta)$ for $\cos\left(\theta_{\mathrm{cm}}^{\eta}\right)$ from -0.75 to 0.15.

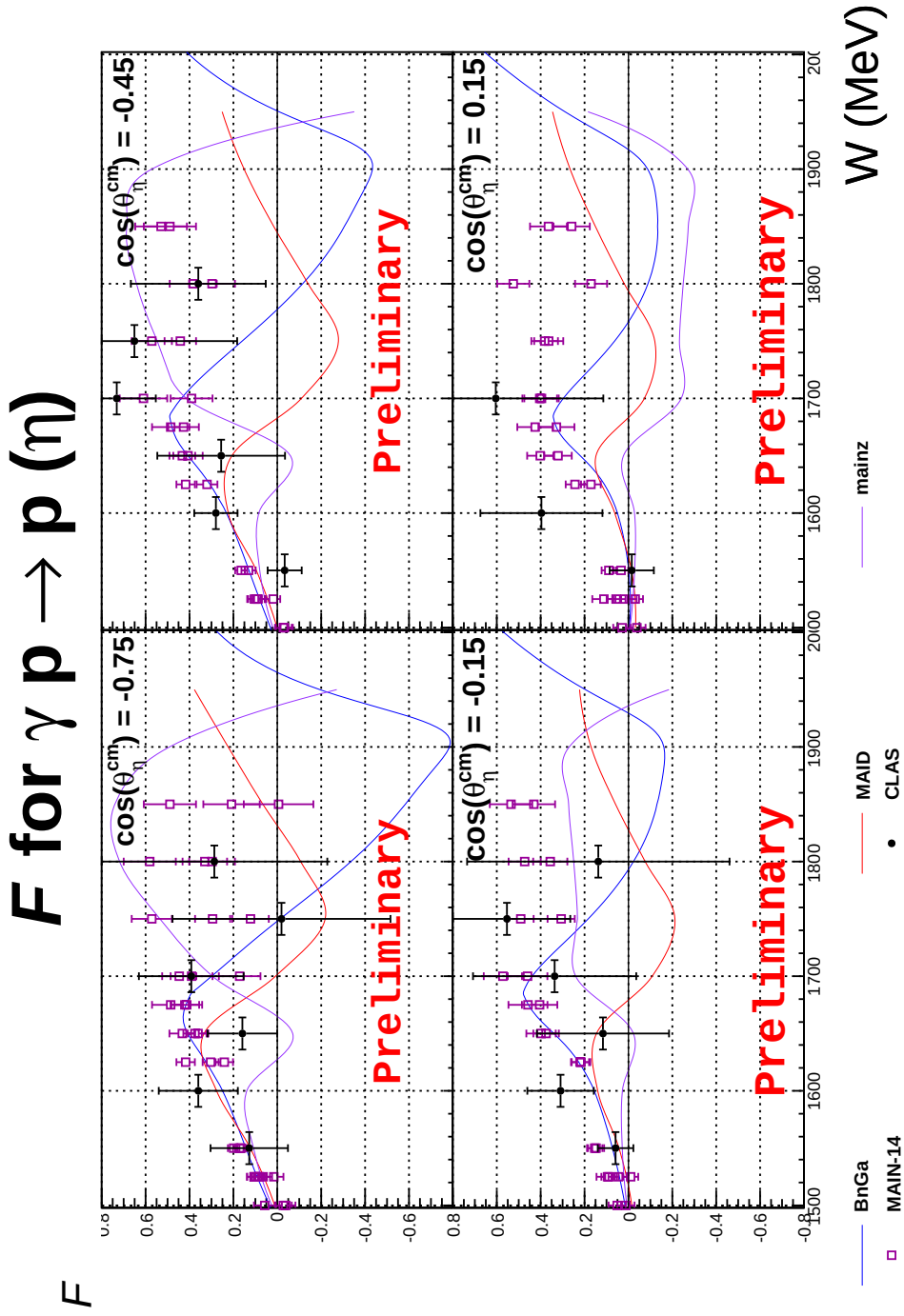

Figure 5.4: The F observable versus W for the process $\gamma p \to p(\eta)$ for $\cos\left(\theta^{\eta}_{\mathrm{cm}}\right)$ from -0.75 to 0.15.

Chapter 6

CONCLUSIONS

The results presented in this dissertation help to clarify the nucleon excitation spectrum and therefore improve understanding of the strong nuclear force. Transverse target asymmetry T and target-beam asymmetry F were found for the reaction $\gamma p \to p\eta$ for center-of-mass energies W from 1.55 to 1.80 GeV with a large angular coverage, which was compared with the only other existing measurements. Until new partial-wave analyses are performed, no changes to the excitation spectrum can be inferred with certainty. Past additions to the world data set have resulted in large changes to the Bonn-Gachina, Mainz, and SAID values for asymmetry predictions. For example, considering the T plots, the BnGa curve incorporated the MAIN-14 data, so it agrees with higher-energy predictions much closer than the MAID or Mainz curves. It is expected that the incorporation of the data from this dissertation will help refine theoretical predictions.

6.1 Future Work

Further theoretical predictions for T and F for η photoproduction should be obtained. Comparisons with the data will then become useful. A collaboration between Arizona State University and theorists at the University of Georgia is presently (at the time of writing) moving forward with such an analysis, as well as with the MAID theorists. The CLAS g9b run period also took data with a linearly-polarized photon beam on the transversely polarized target. With these conditions, it should be possible to measure the observables of target polarization asymmetry P and make a measurement of the double-polarization observable H. The data from this dissertation on the T and F observables, along with data from the other six observables obtainable from CLAS experiments (σ, Σ, G, E, P, and

H) will form a nearly-complete set, which can almost completely specify the process of η-meson photoproduction from the proton in the W range of these measurements, $W =$ 1.55 to 1.80 GeV and therefore help to clarify the nucleon excitation spectrum.

REFERENCES

[1] Image by MissMJ, distributed under a CC BY 3.0 license.

[2] S. K. Choi, *et al.* (Belle Collaboration), Phys. Rev. Lett. **100**, 142001 (2008). DOI:10.1103/PhysRevLett.100.142001

[3] V. M. Abazov, *et al.* (D0 Collaboration), Phys. Rev. Lett. (to be published). arXiv:1602.07588v2 [hep-ex]

[4] J. van Tilburg (LHCb Collaboration), in Proceedings of the 51st Rencontres de Moriond on Electroweak Interactions and Unified Field Theories, 2016, edited by J. Dumarchez and E. Augé (unpublished). cds.cern.ch/record/2069134

[5] Fu-Guang Cao, Phys. Rev. D **85**, 057501 (2012). DOI:10.1103/PhysRevD.85.057501

[6] S. Capstick and N. Isgur, Phys. Rev. D **34**, 34 (1986). DOI:10.1103/PhysRevD.34.2809

[7] K. A. Olive *et al.* (Particle Data Group), Chin. Phys. C **38**, 090001 (2014). pdg.lbl.gov

[8] Nuclear Science Advisory Committee, *2015 NSAC Long Range Plan*, 18 September 2015. science.energy.gov/~/media/np/nsac/pdf/2015LRP/2015_LRPNS_091815.pdf

[9] F. J. Klein *et al.* (CLAS Collaboration), in *AIP Conference Proceedings* **1432**, 51 (2011). DOI:10.1063/1.3701188

[10] M. Dugger, Ph.D. thesis, Arizona State University, 2001. www.jlab.org/Hall-B/general/thesis/Dugger_thesis.pdf

[11] P. Collins, Ph.D. thesis, Arizona State University, 2009. www.jlab.org/Hall-B/general/thesis/Collins_thesis.pdf

[12] B. Morrison, Ph.D. thesis, Arizona State University, 2011. hdl.handle.net/2286/R.A.93211

[13] P. Levi Sandri *et al.*, Eur. Phys. J. A **51**, 77 (2015). arXiv:1407.6991v2

[14] R. L. Walker, Phys. Rev. **182**, 1729 (1969). DOI:10.1103/PhysRev.182.1729

[15] I. S. Barker, A. Donnachie, and J. K. Storrow, Nucl. Phys. B **95**, 347 (1975). DOI:10.1016/0550-3213(75)90049-8

[16] H. Olsen and L.C. Maximon, Phys. Rev. **114**, 887 (1959). DOI:10.1103/PhysRev.114.887

[17] M. L. Swartz, SLAC-PUB-4656, 1988 (unpublished). `www.slac.stanford.edu/cgi-wrap/getdoc/slac-pub-4656.pdf`

[18] C. D. Keith *et al.*, Nucl. Inst. Meth. A **684**, 27 (2012). DOI:10.1016/j.nima.2012.04.067

[19] A. W. Overhauser, Phys. Rev. **92**, 2 (1953). DOI:10.1103/PhysRev.92.411

[20] M. Poelker, Appl. Phys. Lett. **67**, 2762 (1995). DOI:10.1063/1.114585

[21] B. A. Mecking *et al.* (CLAS Collaboration), Nucl. Instr. Meth. A **503**, 513 (2003). DOI:10.1016/S0168-9002(03)01001-5

[22] D. I. Sober *et al.*, Nucl. Instr. Meth. A **440**, 263 (2000). DOI:10.1016/S0168-9002(99)00784-6

[23] E. S. Smith *et al.*, Nucl. Instr. Meth. A **432**, 265 (1999). DOI:10.1016/S0168-9002(99)00484-2

[24] M. D. Mestayer *et al.*, Nucl. Instr. Meth. A **449**, 81 (2000). DOI:10.1016/S0168-9002(00)00151-0

[25] E. Pasyuk, CLAS NOTE 2007–008, 2007 (unpublished).

[26] F. Klein and N. Walford, (unpublished). `clasweb.jlab.org/rungroups/g9/wiki/index.php/TSCtimeCorr`

[27] M. Dugger, (unpublished). `userweb.jlab.org/~dugger/frost/newPID.pdf`

[28] M. Dugger, (unpublished). `userweb.jlab.org/~dugger/frost/pid2andTof.pdf`

[29] R. Tucker, (unpublished). `userweb.jlab.org/~rtucker/asu/FROST-1406.pdf`

[30] R. Tucker (unpublished). `userweb.jlab.org/~rtucker/asu/FROST-1406b.pdf`

[31] E. Pasyuk, CLAS NOTE 2007–016, 2007 (unpublished).

[32] M. Dugger *et al.*, CLAS NOTE 2013–011, 2013 (unpublished).

[33] P. Roy, FROST group meeting, July 17th 2013, 2013 (unpublished).

[34] Phi fits available at `userweb.jlab.org/~rtucker/asu/phi_fits/`.

[35] Jones E, Oliphant E, Peterson P, *et al.*, *SciPy: Open Source Scientific Tools for Python*, 2001–. `www.scipy.org`

[36] C. S. Akondi *et al.* (A2 Collaboration), Phys. Rev. Lett. **113**, 102001 (2014). DOI:10.1103/PhysRevLett.113.102001

[37] D. Drechsel, S. S. Kamalov, and L. Tiator, Eur. Phys. J. A **34**, 69 (2007). DOI:10.1140/epja/i2007-10490-6

[38] E. Gutz *et al.* (CBELSA/TAPS Collaboration), Eur. Phys. J. A **50**, 74 (2014). DOI:10.1140/epja/i2014-14074-1

[39] R. A. Arndt, W. J. Briscoe, M. W. Paris, I. I. Strakovsky, R. L. Workman, Chin. Phys. C **33**, 1063 (2009). DOI:10.1088/1674-1137/33/12/004

[40] The full database and numerous partial-wave analyses can be accessed at the SAID Web site: `gwdac.phys.gwu.edu`.

APPENDIX A

T OBSERVABLE FOR η PHOTOPRODUCTION

Table A.1: T observable for η photoproduction as a function of the center-of-mass energy W in MeV and the cosine of the center-of-mass η-meson scattering angle $\theta_\eta^{\mathrm{cm}}$.

W	$\cos\theta_\eta^{\mathrm{cm}}$	T	σ_T
1550	−0.75	0.1287	0.0249
1550	−0.45	0.1560	0.0127
1550	−0.15	0.1585	0.0140
1550	0.15	0.1769	0.0188
1600	−0.75	0.2132	0.0310
1600	−0.45	0.2164	0.0263
1600	−0.15	0.2414	0.0306
1600	0.15	0.1367	0.0597
1650	−0.75	0.2631	0.0308
1650	−0.45	0.3184	0.0517
1650	−0.15	0.5309	0.0669
1700	−0.75	0.4950	0.0561
1700	−0.45	0.1710	0.0894
1700	−0.15	0.2750	0.1126
1750	−0.75	0.5495	0.1227
1750	−0.45	0.5681	0.1186
1750	−0.15	0.3563	0.0926
1750	0.15	0.3671	0.1440
1800	−0.75	0.0414	0.2398
1800	−0.45	0.1967	0.1172
1800	−0.15	0.0273	0.1582
1800	0.15	0.6022	0.1971

APPENDIX B

F OBSERVABLE FOR η PHOTOPRODUCTION

Table B.1: F observable for η photoproduction as a function of the center-of-mass energy W in MeV and the cosine of the center-of-mass η-meson scattering angle $\theta_\eta^{\mathrm{cm}}$.

W	$\cos\theta_\eta^{\mathrm{cm}}$	F	σ_F
1550	−0.75	0.1278	0.1763
1550	−0.45	−0.0336	0.0776
1550	−0.15	0.0587	0.0811
1550	0.15	−0.0151	0.1006
1600	−0.75	0.3599	0.1802
1600	−0.45	0.2798	0.0986
1600	−0.15	0.3094	0.1514
1600	0.15	0.3965	0.2782
1650	−0.75	0.1591	0.1583
1650	−0.45	0.2558	0.2909
1650	−0.15	0.1162	0.3011
1700	−0.75	0.3918	0.2387
1700	−0.45	0.7315	0.1779
1700	−0.15	0.3364	0.3719
1700	0.15	0.6046	0.4901
1750	−0.75	−0.0191	0.4964
1750	−0.45	0.6509	0.4680
1750	−0.15	0.5535	0.2886
1750	0.15	0.1287	0.5564
1800	−0.75	0.2869	0.5147
1800	−0.45	0.3599	0.3072
1800	−0.15	0.1374	0.5979